Black carbon aerosol over the Los Angeles Basin during CalNex

A. R. Metcalf,[1] J. S. Craven,[2] J. J. Ensberg,[2] J. Brioude,[3] W. Angevine,[3] A. Sorooshian,[4,5] H. T. Duong,[4] H. H. Jonsson,[6] R. C. Flagan,[1,2] and J. H. Seinfeld[1,2]

Received 1 December 2011; revised 13 March 2012; accepted 14 March 2012; published 20 April 2012.

[1] Refractory black carbon (rBC) mass and number concentrations were quantified by a Single Particle Soot Photometer (SP2) in the CalNex 2010 field study on board the Center for Interdisciplinary Remotely-Piloted Aircraft Studies (CIRPAS) Twin Otter in the Los Angeles (LA) Basin in May, 2010. The mass concentrations of rBC in the LA Basin ranged from 0.002–0.530 μg m^{-3}, with an average of 0.172 μg m^{-3}. Lower concentrations were measured in the Basin outflow regions and above the inversion layer. The SP2 afforded a quantification of the mixing state of rBC aerosols through modeling the scattering cross-section with a core-and-shell Mie model to determine coating thickness. The rBC particles above the inversion layer were more thickly coated by a light-scattering substance than those below, indicating a more aged aerosol in the free troposphere. Near the surface, as the LA plume is advected from west to east with the sea breeze, a coating of scattering material grows on rBC particles, coincident with a clear growth of ammonium nitrate within the LA Basin and the persistence of water-soluble organic compounds as the plume travels through the outflow regions. Detailed analysis of the rBC mixing state reveals two modes of coated rBC particles; a mode with smaller rBC core diameters (~90 nm) but thick (>200 nm) coating diameters and a mode with larger rBC cores (~145 nm) with a thin (<75 nm) coating. The "weekend effect" in the LA Basin results in more thickly coated rBC particles, coinciding with more secondary formation of aerosol.

Citation: Metcalf, A. R., J. S. Craven, J. J. Ensberg, J. Brioude, W. Angevine, A. Sorooshian, H. T. Duong, H. H. Jonsson, R. C. Flagan, and J. H. Seinfeld (2012), Black carbon aerosol over the Los Angeles Basin during CalNex, *J. Geophys. Res.*, *117*, D00V13, doi:10.1029/2011JD017255.

1. Introduction

[2] Black carbon is an important atmospheric constituent owing to its role in both air pollution and climate. Refractory black carbon (rBC), alternatively referred to as elemental carbon, light-absorbing carbon, or simply black carbon, is emitted from a variety of incomplete combustion sources, including diesel and gasoline-burning vehicles, residential fuel use, ships, and biomass burning. rBC refers to the strongly light-absorbing component of soot, which may contain other constituents such as polycyclic aromatic hydrocarbons, aliphatic hydrocarbons, and other volatile compounds. rBC, as defined here, is the quantity reported in emission inventories [*Dentener et al.*, 2006] and simulated in regional air quality models [*Binkowski and Roselle*, 2003]. While the majority of atmospheric particulate chemical constituents primarily scatter sunlight, producing an overall cooling effect on climate, rBC absorbs strongly in visible and ultraviolet wavelengths and is the dominant component of light-absorbing atmospheric aerosol. A significant presence of rBC in ambient aerosol can lead to heating of the atmosphere, with effects on atmospheric transport and cloud dynamics [e.g., *Jacobson*, 2002; *Menon et al.*, 2002; *Chung and Seinfeld*, 2005; *Bond*, 2007; *Ramanathan et al.*, 2007; *Ramanathan and Carmichael*, 2008; *Bauer et al.*, 2010; *Ramana et al.*, 2010; *Jones et al.*, 2011].

[3] After emission, rBC particles generally become coated by inorganic and organic (non-absorbing) components via coagulation with other particles and condensation of vapors [e.g., *Riemer et al.*, 2004]. Fresh urban-emitted rBC has typically been shown to be thinly coated with secondary material, while rBC in aged air masses tends to be more thickly coated [*Johnson et al.*, 2005; *Moteki et al.*, 2007; *Shiraiwa et al.*, 2007, 2008; *Schwarz et al.*, 2008a; *Subramanian et al.*, 2010]. In addition, rBC at higher altitudes is found to be more thickly coated than that near the ground [*Schwarz et al.*, 2008b]. Layers of rBC above reflective clouds have an increased radiative forcing per unit

[1]Division of Engineering and Applied Science, California Institute of Technology, Pasadena, California, USA.
[2]Division of Chemistry and Chemical Engineering, California Institute of Technology, Pasadena, California, USA.
[3]Chemical Sciences Division, NOAA Earth System Research Laboratory, Boulder, Colorado, USA.
[4]Department of Chemical and Environmental Engineering, University of Arizona, Tucson, Arizona, USA.
[5]Department of Atmospheric Sciences, University of Arizona, Tucson, Arizona, USA.
[6]Center for Interdisciplinary Remotely-Piloted Aircraft Studies, Naval Postgraduate School, Monterey, California, USA.

0148-0227/12/2011JD017255

Table 1. Urban Black Carbon Measurement Studies

Region	Dates	BC Levels[a] ($\mu g\ m^{-3}$)	Measurement Method	Reference
Asia				
Sapporo, Japan	1982	5.1 (2.3–8.0)	ground, filter	*Ohta and Okita* [1990]
Nagoya, Japan	1984–1986	5.3–34.4	ground, filter	*Kadowaki* [1990]
Uji, Japan	1989–1999	2.6	ground, filter	*Hitzenberger and Tohno* [2001]
Sapporo, Japan	1991–1992	3.9 (2.25–6.93)	ground, filter	*Ohta et al.* [1998]
Seoul, Korea	1994	7.6 (4.86–9.86)	ground, filter	*Kim et al.* [1999]
Kaohsiung City, Taiwan	1998–1999	2.2–5.2	ground, filter	*Lin and Tai* [2001]
Mumbai, India	1999	7.5–17.5	ground, filter	*Venkataraman et al.* [2002]
Seoul, Korea	1999	8.4	ground, filter	*Park et al.* [2001]
Beijing, China	1999–2000	6.3–11.1	ground, filter	*He et al.* [2001]
Bangalor, India	2001	0.4–10.2	ground, aethalometer	*Babu et al.* [2002]
Guangzhou, China	2004	7.1 (3.1–19.4)	ground, filter	*Andreae et al.* [2008]
Kanpur, India	2004	6–20	ground, aethalometer	*Tripathi et al.* [2005]
Nagoya, Japan	2004	0.5–1.1	aircraft, SP2	*Moteki et al.* [2007]
Europe				
Orleans, France	1985	2.9	ground, filter	*Del Delumyea and Kalivretenos* [1987]
Paris, France	1985	7.9	ground, filter	*Del Delumyea and Kalivretenos* [1987]
Clermont, France	1985	2.4	ground, filter	*Del Delumyea and Kalivretenos* [1987]
Strasbourg, France	1985	2.9	ground, filter	*Del Delumyea and Kalivretenos* [1987]
Görlitz, Germany	1988–1990	1.3–11.8	ground, filter	*Zier* [1991]
Halle, Germany	1988–1990	1.6–12.0	ground, filter	*Zier* [1991]
Kap Arkona, Germany	1988–1990	0.4–3.5	ground, filter	*Zier* [1991]
Neuglobsow, Germany	1988–1990	0.6–5.2	ground, filter	*Zier* [1991]
Neuhaus, Germany	1988–1990	0.5–3.5	ground, filter	*Zier* [1991]
Potsdam, Germany	1988–1990	1.0–12.3	ground, filter	*Zier* [1991]
Radebeul, Germany	1988–1990	1.4–12.6	ground, filter	*Zier* [1991]
Dushanbe, Russia	1989	4–20	ground, filter	*Hansen et al.* [1993]
Vienna, Austria	1989–1999	2.8	ground, filter	*Hitzenberger and Tohno* [2001]
Arnhem, Netherlands	1994	2.95	ground, filter	*Janssen et al.* [1997]
Po Valley, Italy	1996	1.0 (0.5–1.5)	ground, filter	*Zappoli et al.* [1999]
Paris, France	1997	13.6	ground, filter	*Ruellan and Cachier* [2001]
Thessaloniki, Greece	1997	3.3	ground, filter	*Ruellan and Cachier* [2001]
Thessaloniki, Greece	1997	3.5–8.9	ground, filter	*Chazette and Liousse* [2001]
Liverpool/Manchester, England	2008	0.3	aircraft, SP2	*McMeeking et al.* [2010]
Barcelona, Spain	2009	1.7 (0.7–3.8)	ground, absorption	*Reche et al.* [2011]
Bern, Switzerland	2009	3.5 (1.3–7.1)	ground, absorption	*Reche et al.* [2011]
Huelva, Spain	2009	0.7 (0.1–2.3)	ground, absorption	*Reche et al.* [2011]
London, England	2009	1.9 (0.8–3.4)	ground, aethalometer	*Reche et al.* [2011]
Lugano, Switzerland	2009	1.8 (0.6–3.6)	ground, absorption	*Reche et al.* [2011]
Santa Cruz de Tenerife, Spain	2009	0.8 (0.1–2.6)	ground, absorption	*Reche et al.* [2011]
Paris, France	2010	1.66	ground, aethalometer	*Healy et al.* [2012]
North America				
Akron, Ohio	1985	2.6	ground, filter	*Del Delumyea and Kalivretenos* [1987]
Chicago, Illinois	1985	4.6	ground, filter	*Del Delumyea and Kalivretenos* [1987]
Norfolk, Virginia	1985	3.0	ground, filter	*Del Delumyea and Kalivretenos* [1987]
Chicago, Illinois	1994–1995	0.19–0.45	ground, filter	*Offenberg and Baker* [2000]
Baltimore, Maryland	1997	0.53–2.60	ground, filter	*Brunciak et al.* [2001]
Atlanta, Georgia	1999	1.5 (0.5–3.0)	ground, filter	*Modey et al.* [2001]
Mexico City, Mexico	2003, 2005	0.5–3.0	ground, SP2	*Baumgardner et al.* [2007]
Dallas/Houston, Texas	2006	0.7 (0.65–0.74)	aircraft, SP2	*Schwarz et al.* [2008a]
Mexico City, Mexico	2006	0.276–1.100	aircraft, SP2	*Subramanian et al.* [2010]
South America				
Santiago, Chile	1991	30.6 (11–75)	ground, filters	*Didyk et al.* [2000]

[a]BC levels are campaign average values (and/or range) depending on availability.

mass relative to those below cloud [*Zarzycki and Bond*, 2010].

[4] Available data indicate that a high fraction of atmospheric rBC particles are mixed with other species [*Pósfai et al.*, 1999; *Park et al.*, 2004; *Seinfeld and Pandis*, 2006; *Schwarz et al.*, 2008a; *Huang et al.*, 2011]. A coating of non-absorbing components onto rBC increases the light scattering and absorption cross sections of these mixed-phase particles [*Fuller et al.*, 1999; *Schnaiter et al.*, 2005; *Bond et al.*, 2006; *Mikhailov et al.*, 2006; *Lack and Cappa*, 2010]. The overall single scattering albedo (the fraction of total light extinction due to scattering) of an internally mixed rBC and non-absorbing aerosol population (all particles of a given size have the same composition) is smaller than that of an externally mixed aerosol population (no mixing of species in individual particles) of the same overall composition and concentration, resulting in a net increase in light absorption by the internally mixed aerosol population. In addition, the mixing state of atmospheric aerosols affects the hygroscopic properties of those aerosols, cloud formation, and atmospheric lifetime by wet deposition [*Weingartner et al.*, 1997; *Jacobson*, 2006]. In short, the extent to which rBC is mixed with non-absorbing aerosol components, such as sulfate, nitrate, and organics, exerts a strong influence on its interaction with radiation and water [*Stier et al.*, 2007; *Cubison et al.*, 2008].

Table 2. California Black Carbon Measurement Studies

Region	Dates	BC Levels[a] (μg m^{-3})	Measurement Method	Reference
Bakersfield area				
Edison	July–September, 1990	2.95	ground, filter	*Chow et al.* [1996]
Caliente	July–September, 1990	3.33	ground, filter	*Chow et al.* [1996]
Bakersfield	May, 2010	0.050 (0.040–0.072)	aircraft, SP2	this study
San Joaquin Valley				
Academy	July–September, 1990	1.43	ground, filter	*Chow et al.* [1996]
Buttonwillow	July–September, 1990	1.86	ground, filter	*Chow et al.* [1996]
San Joaquin Valley	May, 2010	0.041 (0.014–0.087)	aircraft, SP2	this study
Long Beach area				
Long Beach	Jan–Dec, 1982	3.75	ground, filter	*Gray et al.* [1986]
Long Beach	Jun–Sep, 1987	0.99	ground, filter	*Chow et al.* [1994]
Long Beach	May, 2010	0.126 (0.010–0.467)	aircraft, SP2	this study
West Los Angeles Basin				
Lennox	Jan–Dec, 1982	4.51	ground, filter	*Gray et al.* [1986]
Downtown LA	Jan–Dec, 1982	4.87	ground, filter	*Gray et al.* [1986]
West Los Angeles	Jan–Dec, 1982	3.61	ground, filter	*Gray et al.* [1986]
Lennox	Jul–Sep, 1984	1.7	ground, filter	*Turpin et al.* [1991]
Downtown LA	Jun–Sep, 1987	2.37	ground, filter	*Chow et al.* [1994]
Hawthorne	Jun–Sep, 1987	0.70	ground, filter	*Chow et al.* [1994]
Diamond Bar	Jan, 1995–Feb, 1996	3.08	ground, filter	*Kim et al.* [2000]
Downtown LA	Jan, 1995–Feb, 1996	3.81	ground, filter	*Kim et al.* [2000]
West LA Basin	May, 2010	0.175 (0.029–0.526)	aircraft, SP2	this study
Pasadena area				
Azusa	Jan–Dec, 1982	3.30	ground, filter	*Gray et al.* [1986]
Burbank	Jan–Dec, 1982	5.04	ground, filter	*Gray et al.* [1986]
Pasadena	Jan–Dec, 1982	3.95	ground, filter	*Gray et al.* [1986]
Duarte	Jan–Dec, 1983	4.35	ground, filter	*Pratsinis et al.* [1988]
Azusa	Jul–Sep, 1984	4.1	ground, filter	*Turpin et al.* [1991]
Pasadena	Jul–Sep, 1984	2.5	ground, filter	*Turpin et al.* [1991]
Azusa	Jun–Sep, 1987	2.64	ground, filter	*Chow et al.* [1994]
Burbank	Jun–Sep, 1987	2.21	ground, filter	*Chow et al.* [1994]
Pasadena	May, 2010	0.179 (0.097–0.381)	aircraft, SP2	this study
East Los Angeles Basin				
Upland	Jan–Dec, 1982	3.14	ground, filter	*Gray et al.* [1986]
Rubidoux	Jan–Dec, 1982	3.03	ground, filter	*Gray et al.* [1986]
Upland	Jul–Sep, 1984	2.8	ground, filter	*Turpin et al.* [1991]
San Bernardino	Jul–Sep, 1984	1.4	ground, filter	*Turpin et al.* [1991]
Claremont	Jun–Sep, 1987	1.92	ground, filter	*Chow et al.* [1994]
Rubidoux	Jun–Sep, 1987	1.73	ground, filter	*Chow et al.* [1994]
Fontana	Jan, 1995–Feb, 1996	3.49	ground, filter	*Kim et al.* [2000]
Rubidoux	Jan, 1995–Feb, 1996	3.25	ground, filter	*Kim et al.* [2000]
Riverside	Feb–May, 2001	0.5–2.7	ground, aethalometer	*Fine et al.* [2004]
Rubidoux	Jun–Aug, 2001	0.8–3.8	ground, aethalometer	*Fine et al.* [2004]
Claremont	Oct, 2001–Mar, 2002	0.3–5.2	ground, aethalometer	*Fine et al.* [2004]
East LA Basin	May, 2010	0.179 (0.047–0.445)	aircraft, SP2	this study

[a]BC levels are campaign average values (and/or range) depending on availability.

[5] Extensive measurements of rBC in urban locations around the globe exist (see Table 1). Wide variability exists in rBC concentrations owing to proximity to emission sources, the environment into and time of year during which the rBC is emitted, the type of combustion source, and the measurement technique used. The extent to which sulfate, nitrate, organics and other species are co-mixed in rBC particles depends on many factors. Sulfate is the dominant secondary component with rBC in many of the locations in which measurements are available. Mexico City and Riverside, CA are two locations, for example, in which nitrate dominates sulfate as the companion species. Regardless of the total concentrations of rBC and other components, the fraction of rBC particles mixed with some amount of secondary material tends to be appreciable in all regions where data are available.

[6] While California has well-documented air quality problems, the state has also taken a leading role in efforts to address air quality and climate change issues. California has ambitious programs to control emissions of pollutants despite the challenges of increased population and demands for goods and services. Studies of the Los Angeles (LA) area are exemplary in terms of the evolution of our understanding of particulate matter in the atmosphere, from the quantification of the contribution of primary emissions from vehicles (diesel and gasoline) [*Schauer et al.*, 1996], to establishing the importance of secondary aerosol formation [*Turpin and Huntzicker*, 1995; *Zhang et al.*, 2007]. Many studies (see Table 2) have measured rBC levels at various locations in California. The first 3D modeling study to treat size-resolved internal mixing of rBC suggested that aerosols containing rBC in LA led to a decrease in daytime surface temperatures but increased nighttime temperatures to a greater extent, causing a net warming [*Jacobson*, 1997]. In the LA Basin, rBC particles are emitted directly from a variety of sources into a rich background of inorganic and organic airborne gaseous and particulate species. Understanding the evolution of rBC-containing particles as they undergo atmospheric

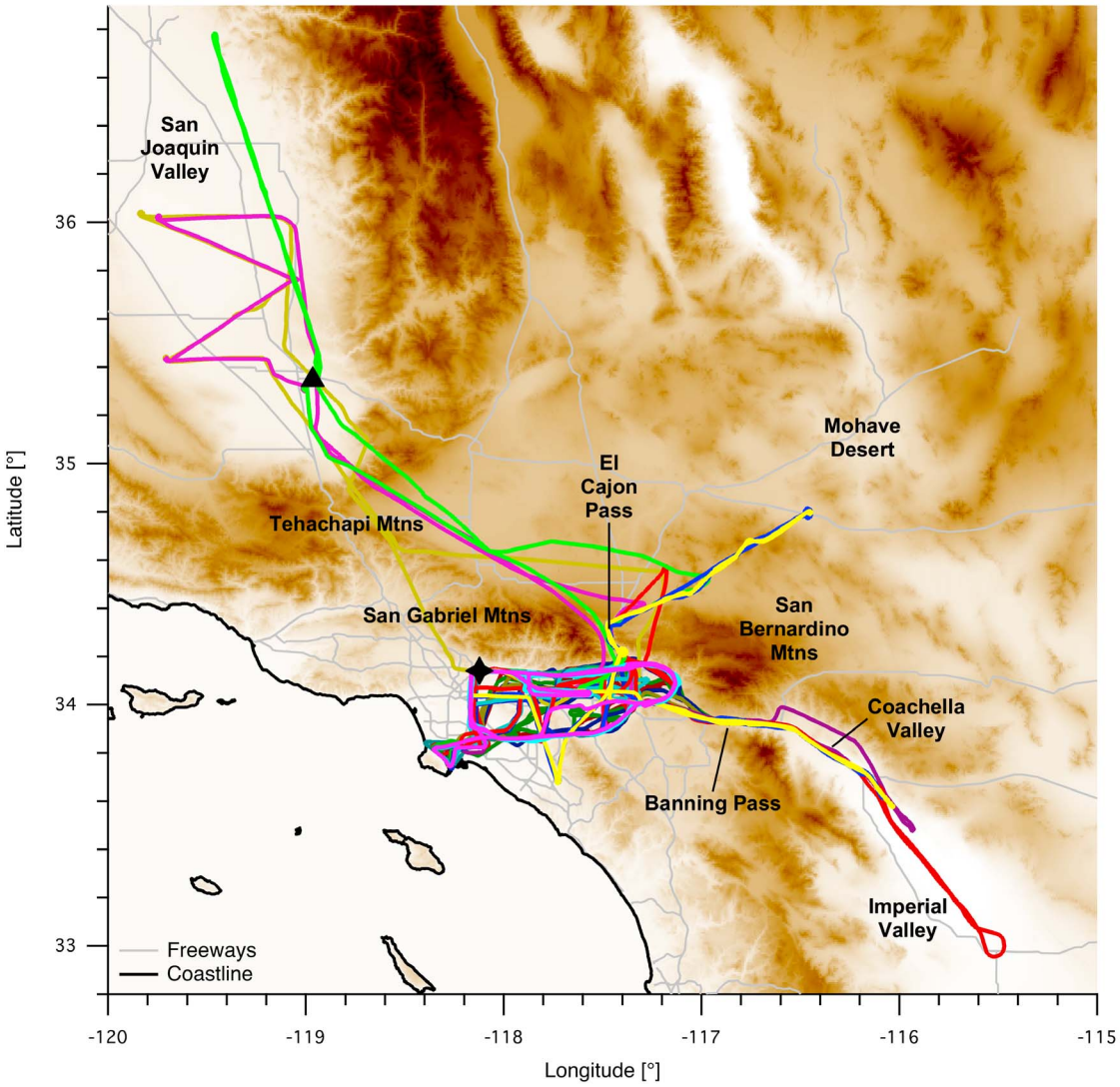

Figure 1. All flight paths (colored lines) of the CIRPAS Twin Otter during CalNex. The star denotes the location of the CalNex LA ground site at Caltech and the triangle denotes the CalNex ground site at Bakersfield. Terrain is shaded brown, with darker colors indicating higher elevation.

aging in this important region provides a unique window on atmospheric gas and particle phase processes.

2. CalNex 2010

[7] The California Research at the Nexus of Air Quality and Climate Change (CalNex) study is a multiagency collaboration aimed at tackling problems related to both air quality and climate change in California (www.esrl.noaa.gov/csd/calnex/). The CalNex study was conducted May–July 2010 in the Los Angeles Basin and southern San Joaquin Valley, involving the NOAA WP-3D aircraft, the CIRPAS Twin Otter aircraft, the NOAA Twin Otter aircraft, the NOAA R/V Ronald H. Brown ship, and two ground-based super-sites, one in Pasadena (34.1405°N, 118.1225°W) on the campus of the California Institute of Technology and one near Bakersfield (35.3463°N, 118.9654°W) in the southern San Joaquin Valley. We report here comprehensive airborne measurements of rBC-containing aerosols in the Los Angeles Basin during May 2010 on the CIRPAS Twin Otter aircraft. Particular focus is paid to rBC concentrations in the Basin, in its outflow regions, and above the inversion layer, as well as the extent to which rBC-containing particles are coated with other species and how this degree of coating varies with location in the Basin and altitude above the surface. The present work is devoted to the actual rBC measurements; subsequent work will address comparison of model predictions and data.

2.1. Climatology of the Los Angeles Basin

[8] The Los Angeles Basin, with a population of about 18 million people, exhibits unique air pollution characteristics and dynamics. Because of the mountainous terrain surrounding the Basin (see Figure 1), airborne species occupy an area of about 1300 km^2, confined near the ground by a relatively shallow day-time mixed layer under 1 km deep [*Robinson*, 1952; *Edinger*, 1959; *Neiburger*, 1969]. The typical daytime sea breeze from the southwest advects emissions toward the north and northeast, exiting the Basin through passes in the

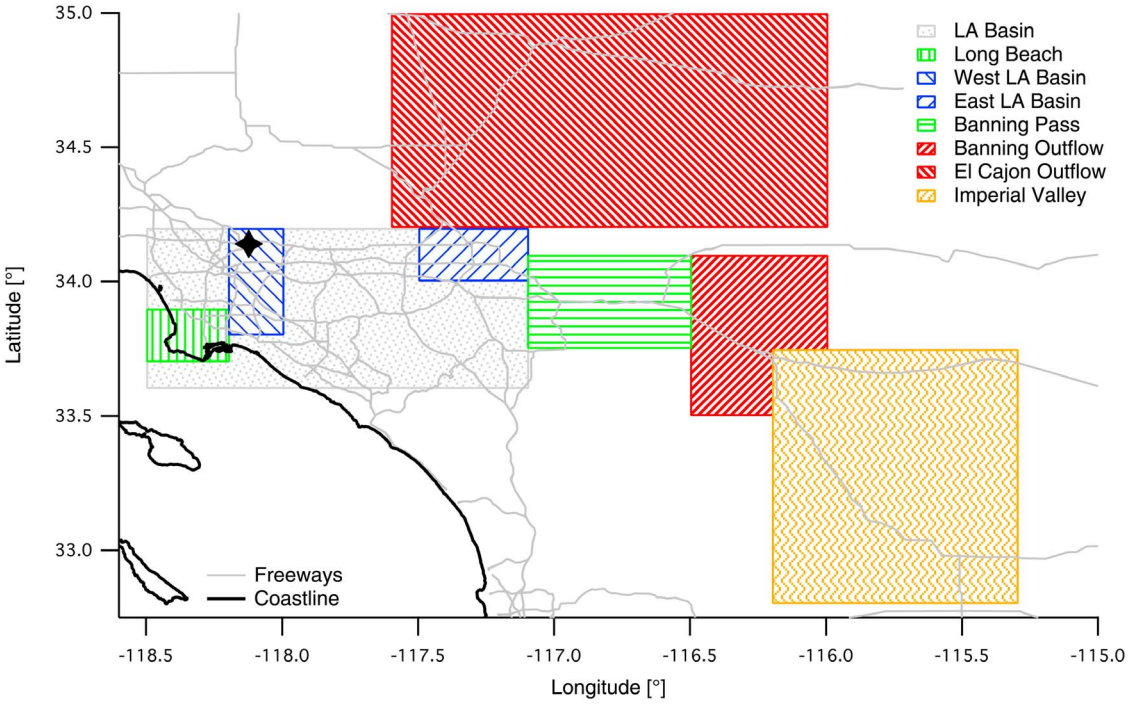

Figure 2. Regional definitions used in Table 4 and elsewhere in the text. Only measurements below the inversion layer are considered.

San Gabriel and San Bernardino mountain ranges to the high desert regions [*Lu and Turco*, 1995]. The two main eastern outflows, the El Cajon and Banning (San Gorgonio) Passes, and one less prominent northern outflow, the Tejon (Newhall) Pass, are not sufficient to completely drain the Basin of its atmospheric contents each day, leading to some degree of carry-over from one day to the next [*Harley et al.*, 2005]. In addition, mountain-flow circulations coupled to the sea breeze can produce multiple layers of pollution in and above the temperature inversion; such layers may mix down to the surface on subsequent days as the boundary layer deepens during its diurnal cycle [*Blumenthal et al.*, 1978; *Wakimoto and McElroy*, 1986; *Moore et al.*, 1991; *Lu and Turco*, 1994, 1995; *Collins et al.*, 2000] or may be subject to long-range transport [*Jaffe et al.*, 1999; *Liu et al.*, 2003; *Liang et al.*, 2004]. Thus, barring a precipitation event, the atmosphere sampled in the LA Basin on any given day contains a mix of fresh and aged material.

[9] For the analysis presented in this work, we have defined several regions of interest in and around the LA Basin (see Figure 2). Given the climatology of the region, we expect the Long Beach and West LA Basin regions to be near major sources of fresh emissions and the Banning Pass and Outflow regions to contain the "LA plume" that has been transported from west to east during the daytime hours.

2.2. FLEXPART Modeling

[10] To track the origins of the specific air masses sampled in the Los Angeles basin during CalNex, a modified version of the FLEXPART Lagrangian particle dispersion model [*Stohl et al.*, 2005] is used to calculate back trajectories of air masses based on advection and turbulent mixing processes. FLEXPART has been used extensively to quantify the impacts of meteorological processes on pollution transport [e.g., *de Foy et al.*, 2006; *Palau et al.*, 2006; *Brioude et al.*, 2009; *Ding et al.*, 2009; *Langford et al.*, 2012]. The main modification for this work consists of using time-averaged winds from the Weather Research Forecasting (WRF version 3.3) meteorology model instead of snapshot winds to improve mass consistency within the FLEXPART model [*Nehrkorn et al.*, 2010]. The WRF output has a spatial grid of 4 km × 4 km, with a temporal resolution of 30 min and 60 vertical levels. In reverse mode, FLEXPART releases virtual tracer particles at receptors, in this case at the instantaneous spatial and temporal location of the Twin Otter aircraft, and integrates their trajectories backward in time using predicted wind fields combined with random turbulent motion. FLEXPART computes the average residence time of the particles in each grid cell (8 km × 8 km) every 2 h over a 24-h period. Surface level contributions to air masses are determined by averaging the residence times of particles between the surface and 200 m altitude.

[11] Figures 3 and 4 present FLEXPART back-trajectory analysis results from three representative flights, May 14 and 15 in Figure 3, and May 25 in Figure 4. In Figure 3, the 12-h integrated residence times reveal the surface history of the air masses sampled in the chosen locations within the LA Basin. The model results for locations on both the western side (Figures 3a and 3b) and the eastern side (Figures 3c and 3d) of the Basin indicate that the dominant airflow in the Basin is the daytime southwesterly sea breeze that advects air masses from Long Beach and downtown LA toward the northeast side of the Basin. FLEXPART results from other LA Basin flights (not shown) paint a similar picture of airflow throughout the LA Basin during the CalNex flights.

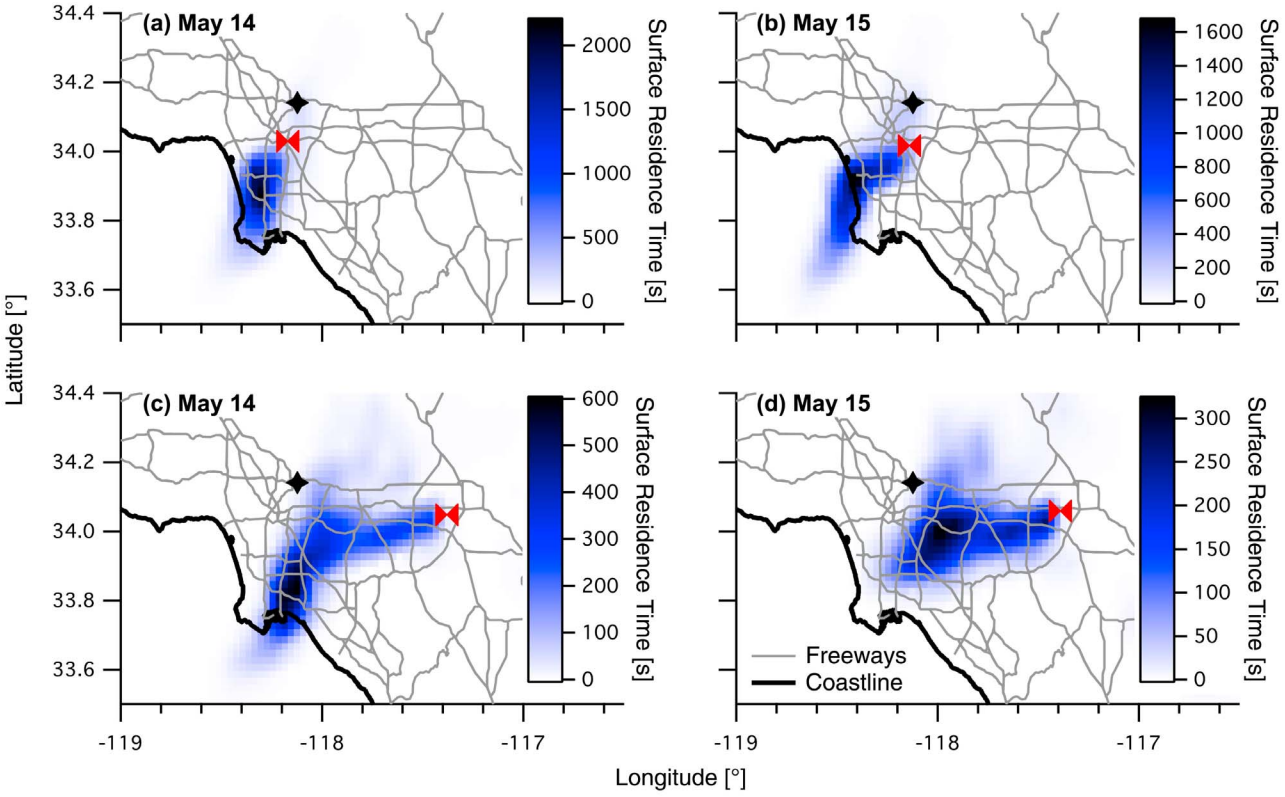

Figure 3. The 12-h integrated surface residence times from FLEXPART during (a and c) the Friday, May 14 flight and (b and d) the Saturday, May 15 flight. Figures 3a and 3b are points on the western side of the LA Basin; Figures 3c and 3d are points on the eastern side of the LA Basin. The red bow-ties denote the location of the Twin Otter aircraft and the stars denote the CalNex LA ground site at Caltech.

[12] Figure 4 displays the FLEXPART results for several locations on the May 25 flight. The left panels are the surface residence times at 4 h prior to sampling and the right panels are the 12-h integrated surface residence times. Figures 4a and 4b show a location approximately halfway between the El Cajon Pass and the farthest sampling point in the El Cajon Outflow region. The surface contribution clearly tails back toward the El Cajon Pass, showing the connection between the LA Basin and the El Cajon Outflow. Figures 4c and 4d show the farthest sampling point in the El Cajon Outflow. At this farthest point from the El Cajon Pass, the tail back toward the Pass is faint, showing that, for this particular day, it takes longer than 12 hours for LA Basin air to reach this location. Figures 4e and 4f show back-trajectories for a location in approximately the center of the Banning Outflow region. The 4-h residence times (Figure 4e) clearly show a connection to the Banning Pass and LA Basin. The 12-h integrated residence times (Figure 4f) show this connection in addition to a smaller circulation within the Coachella Valley. The FLEXPART results for the Imperial Valley sampling location, in Figures 4g and 4h, show no connection to the LA Basin, with both the 4-h (Figure 4g) and 12-h integrated (Figure 4h) back-trajectories indicating flow from the southeast.

2.3. Twin Otter Flights

[13] The Center for Interdisciplinary Remotely-Piloted Aircraft Studies (CIRPAS, Naval Postgraduate School, Monterey, CA, USA) Twin Otter conducted a total of 18 research flights during the month of May, 2010 as part of the CalNex field campaign. Figure 1 shows all 18 Twin Otter flight tracks during CalNex, and Table 3 gives a brief synopsis of each flight. All flights originated from the Ontario International Airport (Ontario, CA, USA). Most sampling was performed at an altitude of about 300 m above ground level at an airspeed of about 50 m s^{-1}. Exceptions were the transits over the San Gabriel and Tehachapi Mountains on the way to the CalNex Bakersfield ground site and the southern San Joaquin Valley. All measurements presented in this work are from instruments inside the unpressurized cabin of the Twin Otter. All instruments are serviced by a two-stage diffusion inlet with a transmission efficiency near unity for particle diameters up to about 3.5 μm [*Hegg et al.*, 2005]. Sampling lines inside the cabin are kept reasonably uniform to all instruments, so further corrections for diffusional losses in these lines have not been made. Owing to a hardware adjustment on the SP2 after the second flight, only data from the final 16 of 18 flights during CalNex are presented here.

[14] A typical flight in the LA Basin consisted of two or three counter-clockwise loops around the Basin, beginning in Ontario and traveling west to Pasadena (passing over the CalNex-LA ground site at Caltech) between the 10 and 210 freeways, then heading south to Long Beach along the 710 freeway to do a loop of missed approaches at the Long Beach and Torrance Airports, then east along the 91 freeway

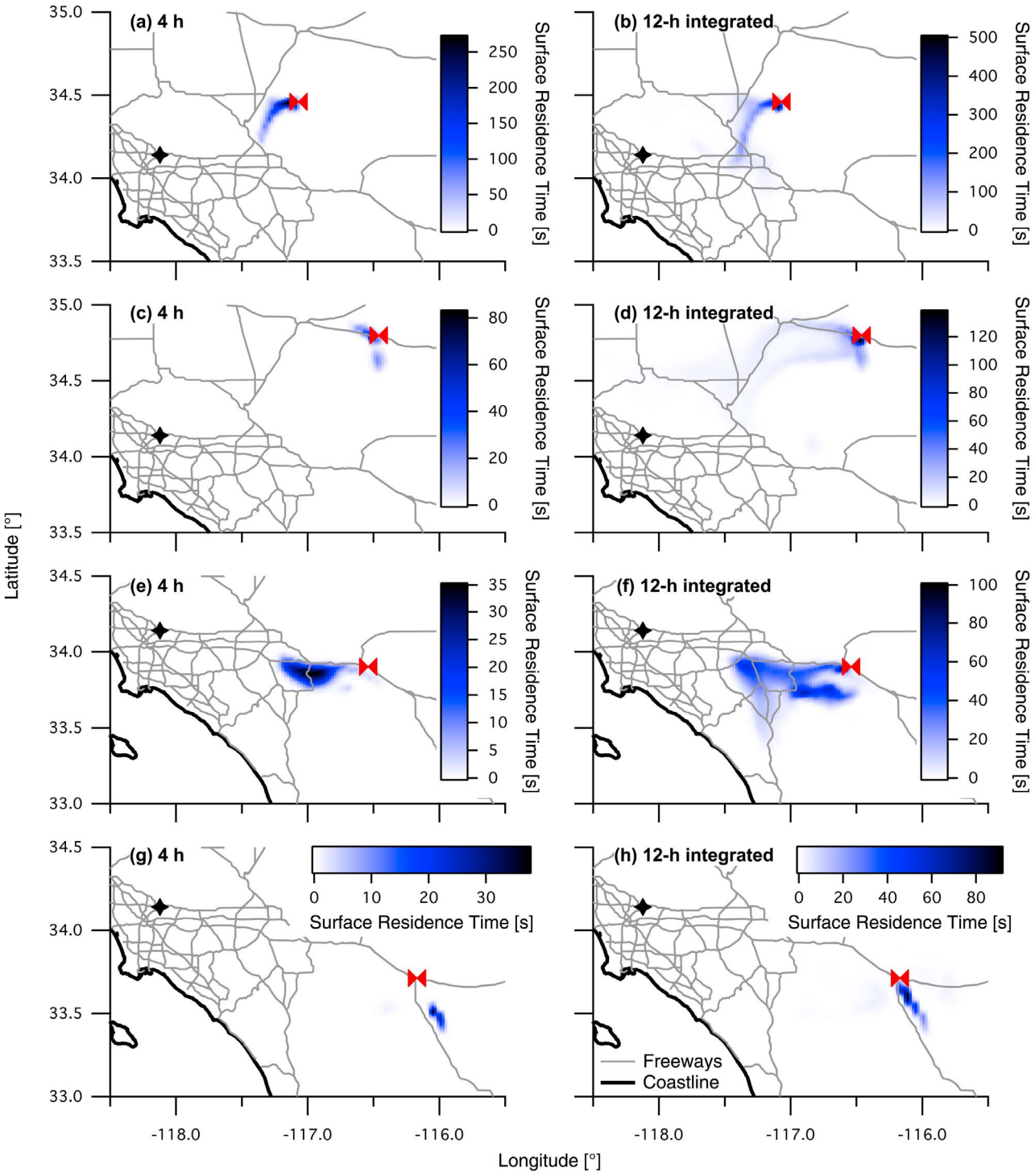

Figure 4. Surface residence time back-trajectories from FLEXPART for the May 25 flight at various regions in the flight: (a and b) midway between the El Cajon Pass and the farthest sampling location in the El Cajon outflow, (c and d) the farthest sampling location in the El Cajon Outflow, (e and f) the Banning Outflow, and (g and h) the Imperial Valley. Figures 4a, 4c, 4e, and 4g are surface residence times at 4 h, showing where the sampled air mass was 4 h prior to sampling. Figures 4b, 4d, 4f, and 4h are 12-h integrated surface residence times, showing the surface contributions for the previous 12 h to the sampled air mass. The red bow-ties denote the location of the Twin Otter aircraft and the stars denote the CalNex LA ground site at Caltech.

Table 3. Summary of CIRPAS Twin Otter Flights During CalNex 2010[a]

Date	Day of Week	Sampling Time (Local Time[b])	Region Sampled
May 4	Tues	11:01–14:23	LA Basin, missed approaches[c]
May 5	Wed	11:04–15:10	LA Basin, missed approaches[c]
May 6	Thu	12:06–15:59	LA Basin
May 7	Fri	11:02–14:57	LA Basin
May 10	Mon	12:00–16:05	LA Basin, western edge
May 12	Wed	10:56–15:08	LA Basin, Imperial Valley
May 13	Thu	11:05–14:54	LA Basin, Imperial Valley
May 14	Fri	10:59–15:01	LA Basin
May 15	Sat	11:13–15:13	LA Basin
May 18	Tue	11:59–15:53	San Joaquin Valley
May 19	Wed	11:40–15:45	LA Basin
May 20	Thu	11:33–15:58	San Joaquin Valley
May 21	Fri	10:57–15:05	LA Basin, outflow regions
May 22	Sat	11:01–15:12	San Joaquin Valley
May 24	Mon	11:01–15:03	LA Basin, outflow regions
May 25	Tue	11:27–15:31	LA Basin, outflow regions
May 27	Thu	10:59–14:45	LA Basin
May 28	Fri	10:58–15:03	LA Basin

[a]The month of May, 2010, in particular, was slightly cooler than normal with a relatively strong coastal marine layer present much of the time. The average high temperature in downtown LA for the month was 19°C, with a maximum high of 24°C on May 29. The average low was 12°C, with the lowest minimum of 10°C on May 25. There were three days (May 17, 18, and 27) with measurable precipitation in downtown LA totaling just 0.11 inches of rain; these days had a particularly strong marine layer leading to measurable drizzle. One day (May 10) had a weak offshore flow, but all others exhibited the typical day-time sea-breeze from the southwest.

[b]Local time is 7 hours behind UTC time.

[c]The missed approaches on the first two flights took place at various small airports scattered throughout the LA Basin. Beginning with May 6 flight, we performed missed approaches only at the Long Beach and Torrance Airports.

to Riverside, turning west along the 210 freeway just before the San Bernardino mountains. During the first two flights, missed approaches were carried out at additional airports throughout the Basin, including Fullerton, Corona, Riverside, Flabob, Banning, Redlands, San Bernardino, Rialto, Cable, Brackett, and El Monte, but these were deemed unnecessary, as little variation in concentrations between an altitude of 15 m and 300 m above ground level were found. Several flights included north–south tracks in order to sample the interior of the Basin, and several flights probed the two main eastern outflows, the El Cajon Pass and the Banning Pass, into the Mohave Desert and Coachella Valley, respectively (see Figure 1).

3. Refractory Black Carbon Measurement

3.1. Single Particle Soot Photometer

[15] rBC mass measurements were made onboard the Twin Otter aircraft with a Droplet Measurement Technologies (DMT, Boulder, CO, USA) Single Particle Soot Photometer (SP2). The SP2 affords measurements of both the particle-by-particle rBC mass as well as the thickness of non-rBC coating on each particle [*Stephens et al.*, 2003; *Baumgardner et al.*, 2004; *Schwarz et al.*, 2006; *Moteki and Kondo*, 2007; *Slowik et al.*, 2007]. The theory of operation and setup of similar SP2 instruments are detailed elsewhere [*Stephens et al.*, 2003; *Schwarz et al.*, 2006, 2010]. Briefly, for each particle traversing the optical cavity of the SP2, 36 μs of signal at 0.2 μs resolution on four detectors, two incandescence and two scattering, are saved for offline analysis. The two incandescence channels detect refractory black carbon mass by measuring the thermal emission from single rBC-containing particles heated to their boiling point when passing through the intense intracavity Nd:YAG laser beam (λ =1064 nm). The two scattering channels detect the scattering cross-section of each particle and are used to determine the mixing state of rBC-containing particles, as detailed below. Note that throughout this work, the rBC volume-equivalent diameter (VED) is calculated from the detected rBC mass by assuming this mass is compacted to a spherical particle with a density of 1.8 g cm^{-3} [*Bond and Bergstrom*, 2006].

[16] Appendix A details the calibration of the Twin Otter SP2. Briefly, the incandescence signals were calibrated with Aquadag (Aqueous Deflocculated Acheson Graphite, Acheson Colloids Company, Port Huron, MI, USA) using the density given by *Gysel et al.* [2011]. The detection range of single-particle rBC mass is 0.48–317 fg (80–696 nm VED). We estimate the uncertainty in mass determination to be ~40%, based largely on the uncertainty in Aquadag mass during calibration, which translates to a ~12% uncertainty in VED. These uncertainties were determined in a similar fashion to previous SP2 studies [*Schwarz et al.*, 2008b; *Shiraiwa et al.*, 2008]. Other rBC standards were tested and the results presented in Appendix A; however, Aquadag is used here because the density is known and samples of Aquadag have been distributed to most SP2 users by DMT, facilitating the inter-comparison of SP2 instruments. Recent results suggest that the SP2 may be up to 40% more sensitive to Aquadag than to ambient rBC particles [*Moteki and Kondo*, 2010; *Laborde et al.*, 2012], but no attempt has been made to correct for this potential bias because it is not yet known how Aquadag relates to ambient rBC particles in the LA Basin. A three-point inter-comparison of the Twin Otter SP2 with the NOAA SP2, which was calibrated with well-characterized Fullerene soot, found that the Twin Otter SP2 response yielded a 12% smaller mass measurement than the NOAA instrument (A. E. Perring, personal communication, 2012). With this potential bias, the mass concentrations reported in this work may be lower than the true ambient values, but the number concentrations are unaffected by this artifact.

[17] The scattering channels were calibrated with dioctyl sebecate (DOS, refractive index = 1.45-0.0*i*), and scattering cross-sections were related to the SP2 signal using Mie theory, as detailed below. For purely scattering ambient particles, we assume a refractive index of 1.5-0.0*i*, in the middle of observed ambient values [*Ensor et al.*, 1972; *Stelson*, 1990; *Stolzenburg et al.*, 1998] and consistent with coating material refractive indices used in this work. The detection range of optical diameter with these assumptions is 169–600 nm. The estimated uncertainty in retrieved scattering amplitude is ~22%, which propagates through Mie theory to an uncertainty of ~5% in optical diameter for purely scattering particles.

3.2. Mixing State Determination

[18] Figure 5 shows the time traces of signal on the four measurement channels of the SP2 for three single particles: an uncoated rBC particle (Figure 5a), a purely scattering particle (Figure 5b), and a coated rBC particle (Figure 5c).

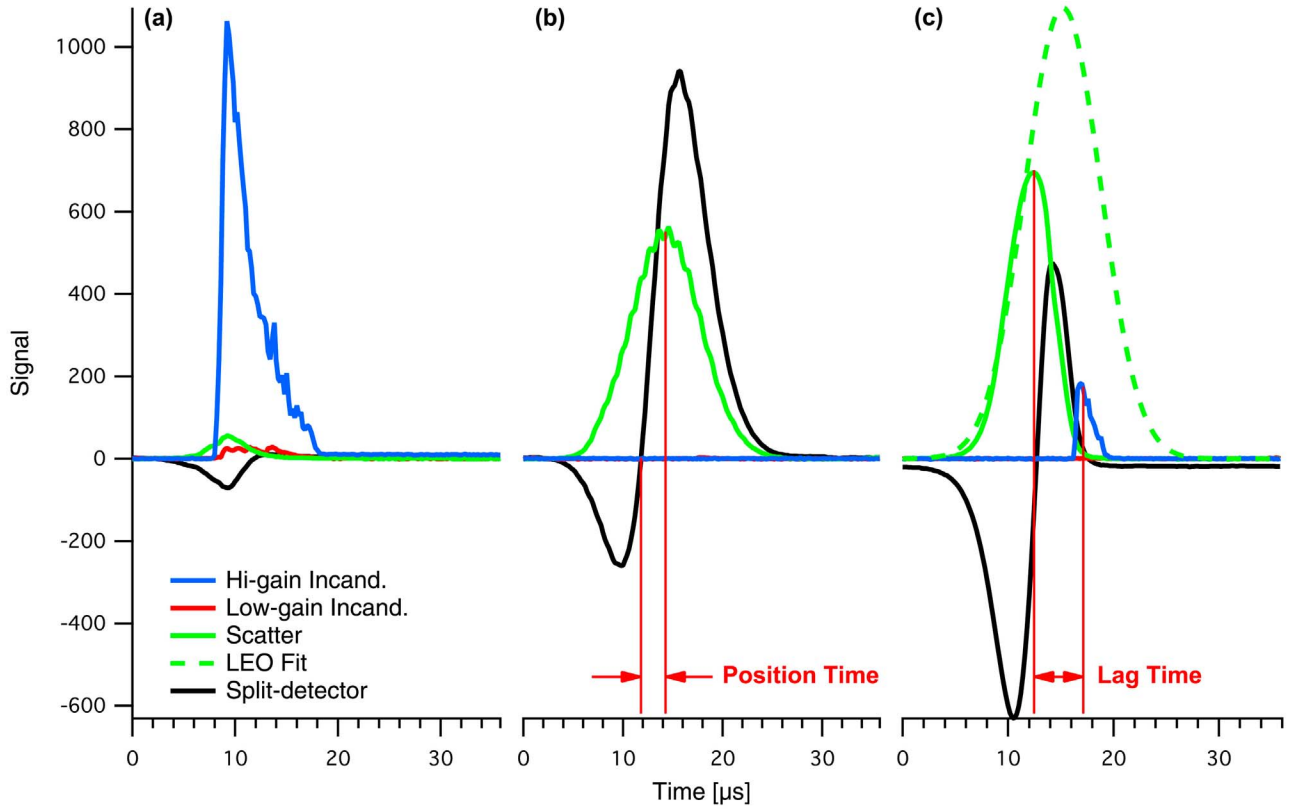

Figure 5. Raw spectra of three single particles measured by the SP2: (a) a 149 nm VED uncoated rBC particle, (b) a 286 nm optical diameter purely scattering particle, and (c) an 83 nm VED rBC core coated by a 237 nm thick layer of a purely scattering substance. "Position Time" labeled in Figure 5b is the time between the zero-crossing of the split-detector signal and the peak of the scatter signal and is used to determine the position of the scatter peak for particles evaporating in the laser beam. "Lag Time" labeled in Figure 5c is the distance between the detected scatter peak and incandescent peak and is used to assess the coating thickness on rBC particles. See the text for a description of the LEO Fit calculation.

An uncoated rBC particle has little or no discernible signal on the scattering channel and, if present, the scattering peak coincides with the incandescent peak, indicating that the scattering arises from the rBC particle itself. A purely scattering particle has no incandescent signal whatsoever, and the scattering signal has the shape of a Gaussian curve. A coated rBC particle exhibits both scattering and incandescing signals.

[19] Typically, as a coated rBC particle heats up in the laser beam of the SP2, the coating material will evaporate, causing the scattering signal to peak and decrease before the onset of the incandescent signal. A parameter often used to describe the coating thickness is the lag time between the peak scattering signal and the peak incandescent signal (labeled in Figure 5c) [*Schwarz et al.*, 2006; *Moteki and Kondo*, 2007]. Previous studies have classified a thickly coated rBC particle as one with a lag time ≥2 μs [*Moteki et al.*, 2007]. In this study, we will classify a thickly coated particle as one with a lag time ≥1.8 μs, a shift of one data point, or time step, in the single-particle data (Figure 5). This shift is made to reflect the observation (not shown) that there are two distinct populations of lag time in the single-particle data for CalNex, similar to the two populations shown by *Moteki et al.* [2007, Figure 3]. A lag time of 1.8 μs is the point that most clearly separates these two populations in our data set.

[20] Because the coating on rBC particles evaporates before the particle passes through the entire laser beam, the scattering signal is not a true Gaussian shape, as in Figure 5b, and is smaller in amplitude than it should be for the full, unperturbed coated rBC diameter (see the difference in Figure 5c). To retrieve an accurate scattering cross-section and, therefore, optical size for this particle, we use the leading-edge only (LEO) part of the scattering signal to fit the scattering data to the calibration, as outlined by *Gao et al.* [2007]. Figure 5c shows a LEO fit compared to the raw signal, which clearly would have under-sized this coated rBC particle had this correction not been made. Appendix A provides more details of how LEO fitting was calibrated and implemented for the Twin Otter SP2.

3.3. Mie Scattering Model

[21] For purely scattering particles detected by the SP2, we calculate scattering cross-section with Mie theory for a given particle diameter and refractive index, for which we have adapted a version of BHMIE [*Bohren and Huffman*, 1998]. This adaptation involves integrating the scattering function over the solid angles subtended by the SP2

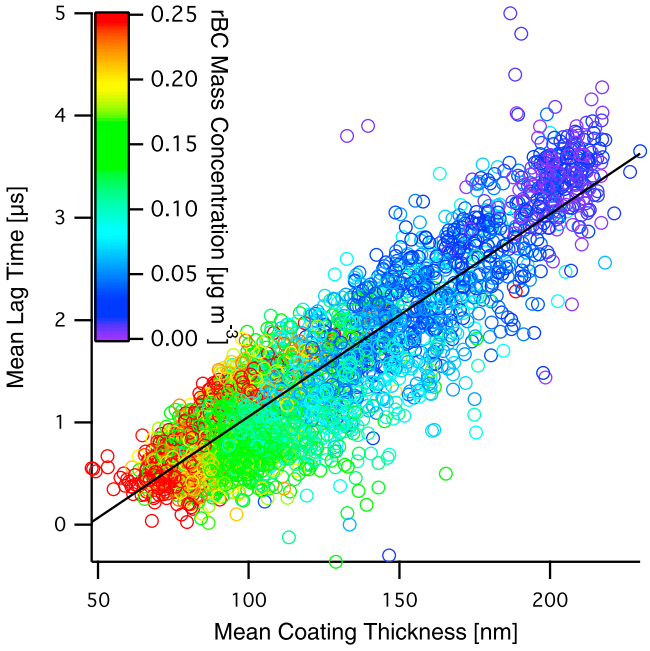

Figure 6. Mean lag time versus mean coating thickness for all 1-min average measurements during CalNex. Marker color indicates rBC mass concentration. Coating thickness is the diameter increase from the rBC VED. The solid black line is a linear fit to the data ($R^2 = 0.797$).

avalanche photodiodes (APDs) to calculate the differential scattering cross-section specifically detected by those APDs rather than the total scattering cross-section. To calculate scattering cross-section for coated rBC particles, we have replaced the scattering coefficients with those for stratified spheres from *Toon and Ackerman* [1981] to create a core-and-shell Mie model. Because the rBC mass is detected with the SP2 incandescence channels, the VED from this mass, with assumed rBC refractive index of 1.95-0.79*i* [*Bond and Bergstrom*, 2006] is treated as a known quantity in the core-and-shell Mie model. An assumed coating refractive index of 1.5-0.0*i*, consistent with earlier published works [*Schwarz et al.*, 2008a, 2008b], leaves coating thickness diameter as the only unknown when comparing measured scattering cross-sections to core-and-shell Mie model scattering cross-sections. The measurements are then fit to the core-and-shell Mie calculations to determine coating thickness diameters. Given an uncertainty in retrieved scattering amplitude of ~22% and an uncertainty in rBC VED of ~12%, uncertainties in coating thicknesses are ~40%, with uncertainty decreasing with increasing coating thickness. For the 1-min average SP2 data, in addition to reporting mean coating thicknesses, the Mie model-derived total coated rBC particle diameter is used to calculate the total particle volume, from which we calculate the coating-only volume by subtracting the calculated rBC core volume.

[22] Previous SP2 studies have emphasized lag time as a way of presenting rBC mixing state [e.g., *Subramanian et al.*, 2010]. Figure 6 relates mean lag times to mean coating thicknesses for all measurements taken during CalNex. The black line is a linear fit of the data ($R^2 = 0.797$; the actual slope and intercept are unimportant) showing a strong correlation between these two variables, as expected. Both measurements are reported because both suffer from limitations. Interpretations of lag times to infer coating thicknesses rely on the aerosol to follow a core-and-shell physical model and for all coatings to evaporate in the SP2 laser at equal rates such that time is related to thickness only and not to coating material as well. Mean coating thicknesses calculated with Mie theory suffer from limited detection range, additional uncertainties in extracting the true scattering peak signal from an evaporating particle, and, again, relies on the core-and-shell physical model to apply.

3.4. The rBC Number and Mass Concentrations

[23] Histograms of single-particle rBC mass onto 500 logarithmically-spaced mass bins between 0.48 and 398 fg (80–750 nm VED) were made for every 1-min of single-particle data. Accumulation mode rBC particle size distributions in the atmosphere have been observed to be single lognormal in nature [*Pueschel et al.*, 1992; *Clarke et al.*, 2004; *Moteki et al.*, 2007; *Schwarz et al.*, 2008a, 2008b]; thus, a single lognormal function is fit to each 1-min number distribution to determine the full distribution over the range of 9.4×10^{-7} to 942 fg (1–1000 nm VED). The fitted mass distributions are implied from the fitted number distributions.

[24] Figure 7 shows examples of typical number and mass distributions measured and fitted for various regions. At very large rBC masses (>300 nm VED), the measurements deviate from the fitted distribution, because at these large masses a single count becomes a significant differential mass (dM) in the distribution. This potential error illustrates the importance of fitting the number distribution to a lognormal, rather than the mass distribution, in order to avoid biasing the fit of the mass distribution. The rBC mass median diameter (MMD) is the VED at the peak of the mass distribution.

[25] The bulk number and mass concentrations are found by integrating each distribution over all sizes and dividing by the sampled volume of air for that 1-min period. The bulk

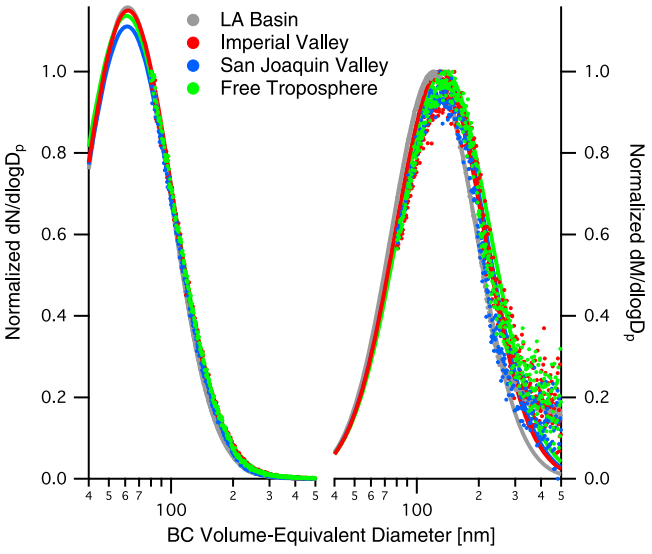

Figure 7. Campaign-average rBC number (left trace) and mass (right trace) distributions by region. Solid lines denote single lognormal fits to the data.

Table 4. Summary of SP2 Measurements Broken Down by Region[a]

Region[b]	rBC Number Concentration (cm^{-3})	rBC Mass Concentration ($\mu g\ m^{-3}$)	Mean Coating Thickness (nm)	Percent Thickly Coated (%)	rBC Mass Fraction (%)	rBC Mass Median Diameter (nm)
LA Basin	267 (288 ± 136)	0.154 (0.167 ± 0.0828)	99 (20)	37 (11)	2.4 (1.3)	122 (7)
Long Beach	187 (199 ± 121)	0.112 (0.126 ± 0.0777)	99 (23)	38 (13)	2.8 (0.9)	130 (7)
Pasadena	289 (321 ± 109)	0.164 (0.179 ± 0.0647)	94 (14)	29 (9)	2.8 (1.2)	120 (3)
West LA Basin	280 (309 ± 149)	0.159 (0.175 ± 0.0873)	93 (20)	32 (10)	2.4 (1.0)	123 (7)
East LA Basin	274 (295 ± 119)	0.159 (0.179 ± 0.0782)	102 (20)	41 (10)	2.1 (1.2)	122 (4)
Banning Pass	162 (162 ± 77)	0.0907 (0.0954 ± 0.0445)	135 (29)	55 (13)	2.0 (1.0)	126 (6)
Basin Outflows	136 (165 ± 104)	0.0792 (0.0978 ± 0.0619)	138 (33)	47 (15)	4.5 (2.3)	127 (7)
Banning Outflow	129 (136 ± 71)	0.0703 (0.0690 ± 0.0265)	144 (28)	54 (15)	4.9 (1.7)	130 (10)
El Cajon Outflow	130 (173 ± 110)	0.0868 (0.105 ± 0.0662)	136 (34)	52 (13)	4.4 (2.3)	129 (7)
Imperial Valley	93 (107 ± 61)	0.0616 (0.0671 ± 0.0293)	156 (17)	65 (8)	5.3 (2.6)	141 (10)
San Joaquin Valley	60 (67 ± 33)	0.0408 (0.0414 ± 0.0143)	153 (20)	58 (13)	1.0 (0.6)	130 (8)
Bakersfield	86 (82 ± 19)	0.0472 (0.0502 ± 0.0102)	145 (14)	52 (6)	1.3 (0.5)	127 (5)
Free Troposphere	14 (54 ± 90)	0.0167 (0.0346 ± 0.0454)	188 (31)	76 (13)	1.7 (2.8)	161 (41)

[a]The concentrations are campaign medians (mean ± 1σ); all other values are campaign-average values (±1σ).
[b]Region definitions are given in Figure 2.

values reported here are derived from the fitted distributions. Uncertainties in the bulk concentrations are dominated by the single-particle mass uncertainty; thus, additional uncertainties due to flow fluctuations are negligible. Because the fitted range captures a wider diameter range than the detection limits of the SP2, the calculated rBC number and mass concentrations are higher than those corresponding to the strict detection range of the instrument. The number concentration nearly doubles because of this adjustment, while the mass concentration is about 15–20% larger.

4. Results and Discussion

4.1. Regional Variability in rBC Aerosol

[26] Over the entire monthlong campaign, rBC mass concentrations in the LA Basin varied from 0.002 to 0.530 $\mu g\ m^{-3}$, with smaller values measured in regions outside of the Basin (see Table 4). rBC-containing particle number concentrations ranged from as low as 3 cm^{-3} up to 1180 cm^{-3}. Figure 8 shows rBC mass concentrations for 12 flights in the LA Basin. On the May 28 flight (Figure 8l), the spikes in mass concentration on the southeast corner of the sampling pattern are the result of flying through a dense smoke plume from a tanker truck fire on the 91 freeway. These spikes have been removed for the calculated values in Tables 2 and 4. The anomalously low concentrations on the southern side of the LA Basin on May 6 (Figure 8a), in the central Basin on May 15 (Figure 8g), and on the northeast corner of the Basin on May 21 (Figure 8i) are a result of sampling above the inversion layer; all other measurements were made at ~300 m above ground level. Figure 9 shows a typical flight contrasting the measurements between the LA Basin and its two eastern outflow regions.

[27] From Figure 8, together with Figure 9a, a pattern of higher rBC mass concentrations occurring on the north side of the Basin emerges. These larger concentrations to the north are the result of a southwesterly sea breeze during the day (see Figure 3) that transports rBC emissions up against the San Gabriel mountains, where the terrain and typically shallow mixed layer collect the air mass prior to exiting the Basin. One might expect enhanced emissions from the Port of Long Beach and the industries (refineries) in the area; however, except for a few spikes in the data near Long Beach, this region is generally characterized by lower concentrations of rBC as compared with the northern side of the LA Basin (see also Table 4).

[28] Table 4 presents a detailed regional breakdown of the SP2 measurements during CalNex. Except for the free troposphere, all measurements are from below the inversion layer, with region definitions given in Figure 2. Within the LA Basin, rBC concentrations are fairly uniform throughout, because the region definitions do not distinguish north and south Basin as discussed above. The rBC mass concentrations in the LA Basin are higher than in the outflow regions (Figure 9a). The mean coating thickness and percent thickly coated both increase from west to east, indicating that the rBC particles are becoming more thickly coated. Moving into the outflows, the rBC continues to become more thickly coated, with the thickest coatings (except for the free troposphere) occurring at the farthest points from the LA Basin (see also Figures 9c and 9d). rBC mass fraction increases in the outflows, despite a decrease in rBC number and mass concentrations, owing to the evaporation of volatile species from the aerosol as the plume is diluted over the desert regions.

[29] Minor differences exist in the mass median diameter of the rBC core aerosol between regions (see Figures 7 and 9b). The MMD is the smallest in the LA Basin, at about 122 nm, indicating the rBC in the Basin is characteristic of fresh urban emissions that tend to have smaller rBC cores [e.g., *McMeeking et al.*, 2010; *Schwarz et al.*, 2008a]. The MMD is smaller by 30–70 nm than most other urban measurements found in the literature [see *McMeeking et al.*, 2010, Table 5]. Most comparable to the Los Angeles values observed are those of fresh rBC emissions at Cranfield airfield in England, which exhibited values near 130 nm [*McMeeking et al.*, 2010], and of the Tokyo, Japan outflow, which exhibited values of 145–150 nm [*Shiraiwa et al.*, 2007]. The MMD of rBC in the Imperial Valley is larger than that in the LA Basin and its outflow regions, indicating an air mass of a different origin. Figures 4g and 4h support this conclusion, showing that the air mass originates from the southeast of its sampling location.

4.2. Secondary Aerosol Chemical Composition

[30] Particle mass and composition measurements were made by an Aerodyne compact time-of-flight aerosol mass spectrometer (C-ToF-AMS, Aerodyne Research, Inc.,

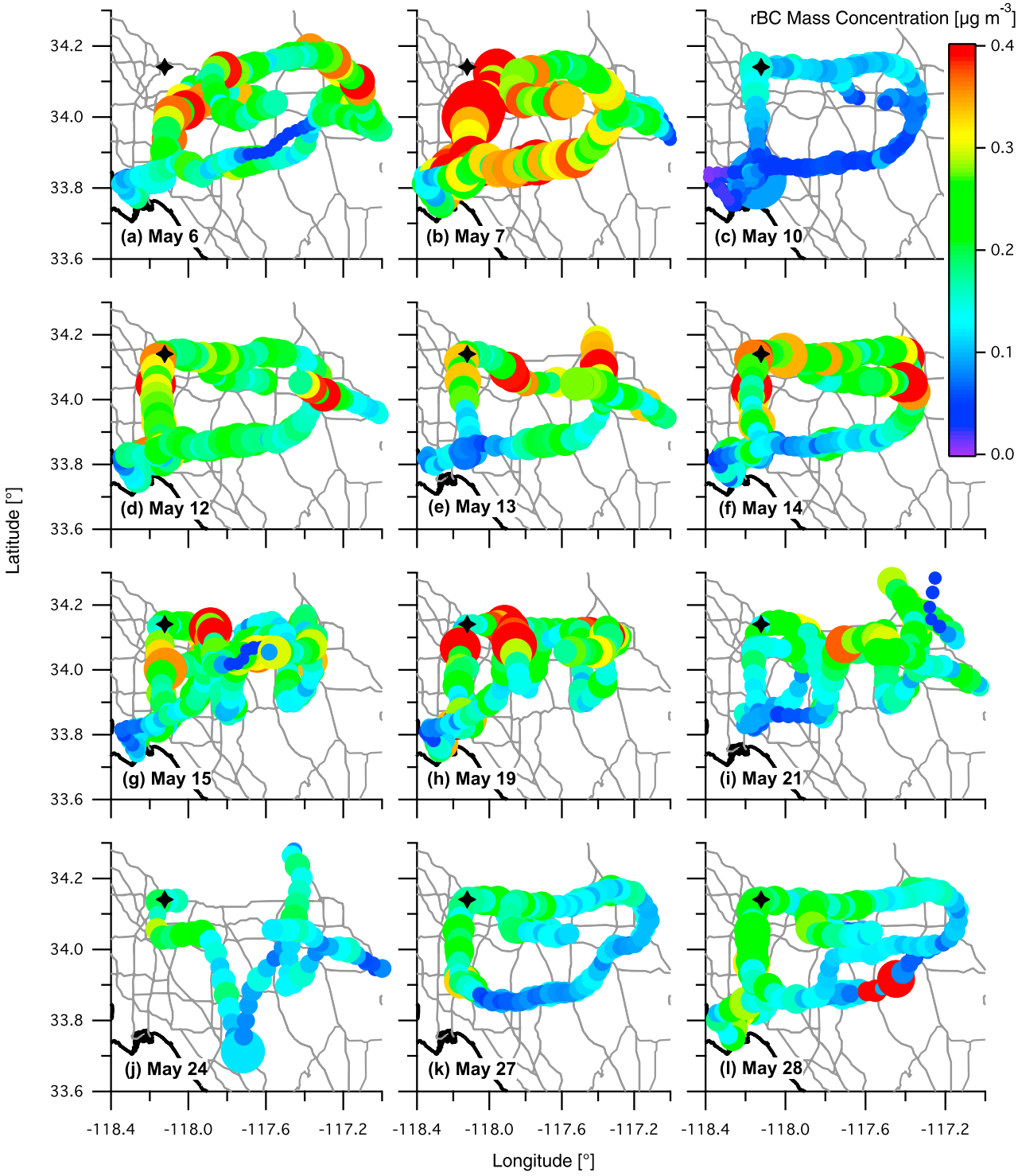

Figure 8. All rBC mass (marker color) and number (marker size) concentrations observed in the LA Basin during CalNex, with the exception of the May 25 flight, which can be found in Figure 9a. The stars denote the CalNex LA ground site at Caltech.

Billerica, MA USA) [*Drewnick et al.*, 2005; *Murphy et al.*, 2009] that was deployed on the final nine Twin Otter flights. The AMS measures sub-micron, non-refractory size-resolved aerosol composition over the diameter range 60 to 600 nm (with unit transmission efficiency) [*Jayne et al.*, 2000]. For the purposes of comparison to SP2 measurements, bulk composition AMS data are averaged to 1-min time intervals. Water-soluble organic carbon (WSOC) was quantified by a particle-into-liquid sampler (PILS; Brechtel Manufacturing, Inc., Hayward, CA) coupled to a Total

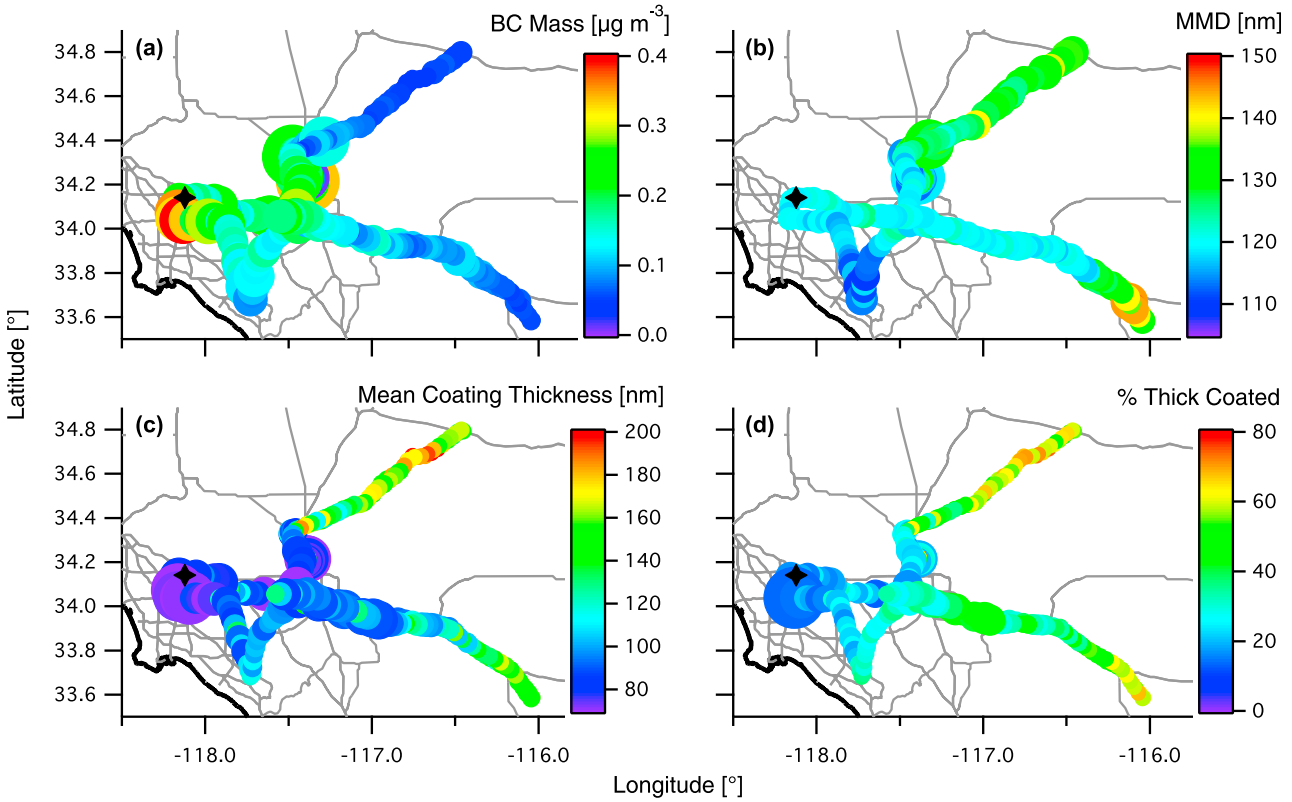

Figure 9. The 1-minute average SP2 data from Research Flight 16 on May 25, 2010: (a) rBC mass (marker color) and number (marker size) concentrations, (b) mass-median diameter of rBC cores (marker color) and width of the mass distributions (marker size), (c) mean coating thickness on rBC particles (marker color) and total volume concentration of the coating on rBC particles in SP2 detection range (marker size), and (d) percent of mixed-phase rBC particles thickly coated (marker color) and number concentration of coated rBC particles in SP2 detection range (marker size). The stars denote the CalNex LA ground site at Caltech.

Organic Carbon (TOC) Analyzer (Sievers Model 800) [*Sullivan et al.*, 2006]. The major findings on the nature of WSOC in Los Angeles during CalNex have been presented elsewhere [*Duong et al.*, 2011]. The WSOC data presented here have been converted to water-soluble organic mass (WSOM) by applying a correction factor of 1.7, which is within range of previous measurements made in Southern California [*Turpin and Lim*, 2001; *Docherty et al.*, 2008; *Wonaschütz et al.*, 2011].

[31] Figure 10 presents the region-averaged ratios of the mass concentration of various chemical species to the rBC mass concentration during the May 25 flight. The regions are ordered from west to east, which coincides with the direction of the general LA airflow; thus, for daytime sampling, plume age increases from left to right on Figure 10 with the exception of the Imperial Valley, which Figures 4g and 4h show to be isolated from the LA Basin for at least the 12 hours prior to measurement. Within the LA Basin, the rBC mass concentration decreases slightly from west to east and decreases sharply in the Banning Outflow and Imperial Valley regions, largely due to dilution of the air mass with the cleaner, desert air. In the absence of any major rBC sources over the desert, rBC can be considered a tracer for the LA plume and the mass ratios reveal the occurrence of secondary formation of these chemical species as the LA plume ages.

[32] The overall mass ratio of measured chemical species to rBC increases from west to east within the LA Basin and is at a maximum in the Banning Pass region, reflecting the build-up of secondary aerosol species, particularly nitrate and organics, relative to rBC. The Banning Pass is a relatively narrow mountain pass on the east side of the LA Basin (see Figures 1 and 2) where the LA plume is advected through this region and out of the Basin by the daytime sea breeze. Figure 9c shows the mean coating thicknesses and Figure 9d shows the percent thickly coated (defined using single-particle lag times) for this flight. Mean coating thicknesses for this flight do not show much increase within the Basin, much like the campaign-average values in Table 4; however, percent thickly coated shows an increase from west to east within the LA Basin with an area of larger percentages in the Banning Pass region. Figure 10 indicates that these more thickly coated particles in the Banning Pass region are likely a mix of ammonium nitrate and organics. A previous study found that coating materials on rBC in Nagoya, Japan were likely ammonium sulfate and secondary organic compounds formed during transport away from the urban center

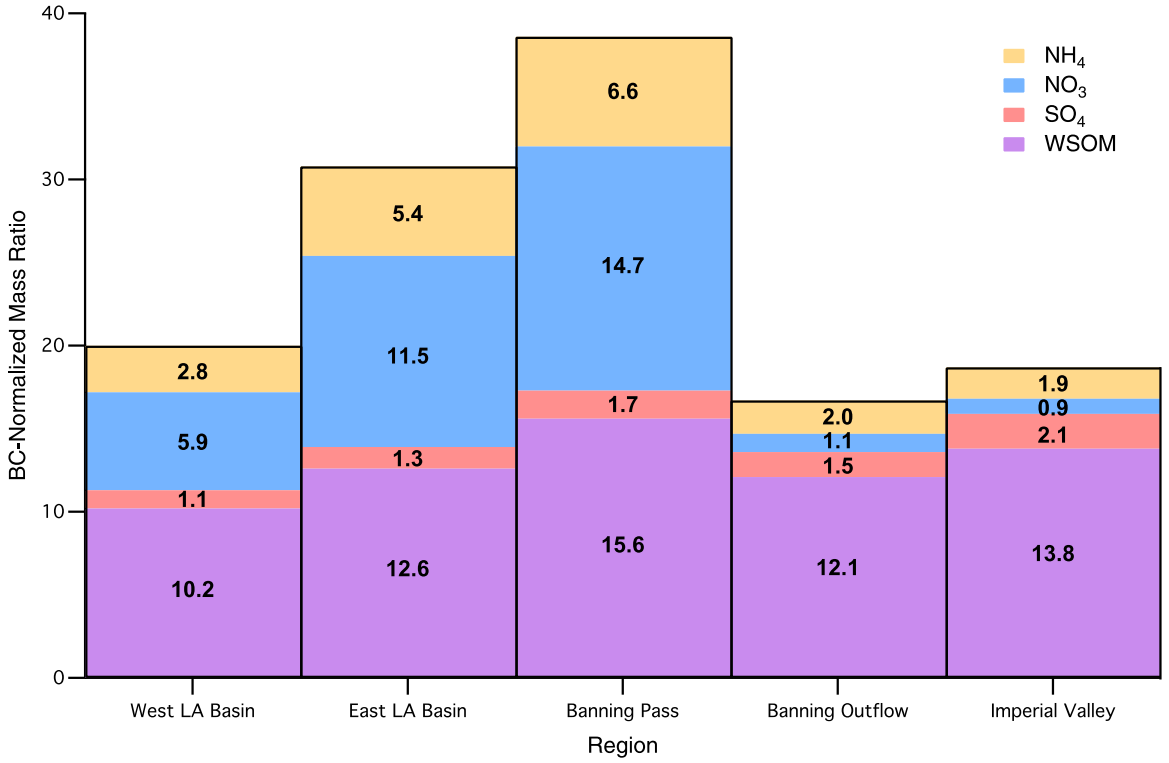

Figure 10. The rBC mass-normalized concentration ratios of aerosol chemical compounds broken down by region from west to east in and near the Los Angeles Basin for the May 25 flight. See text for details on the calculation of water-soluble organic mass (WSOM) and Figure 2 for region definitions.

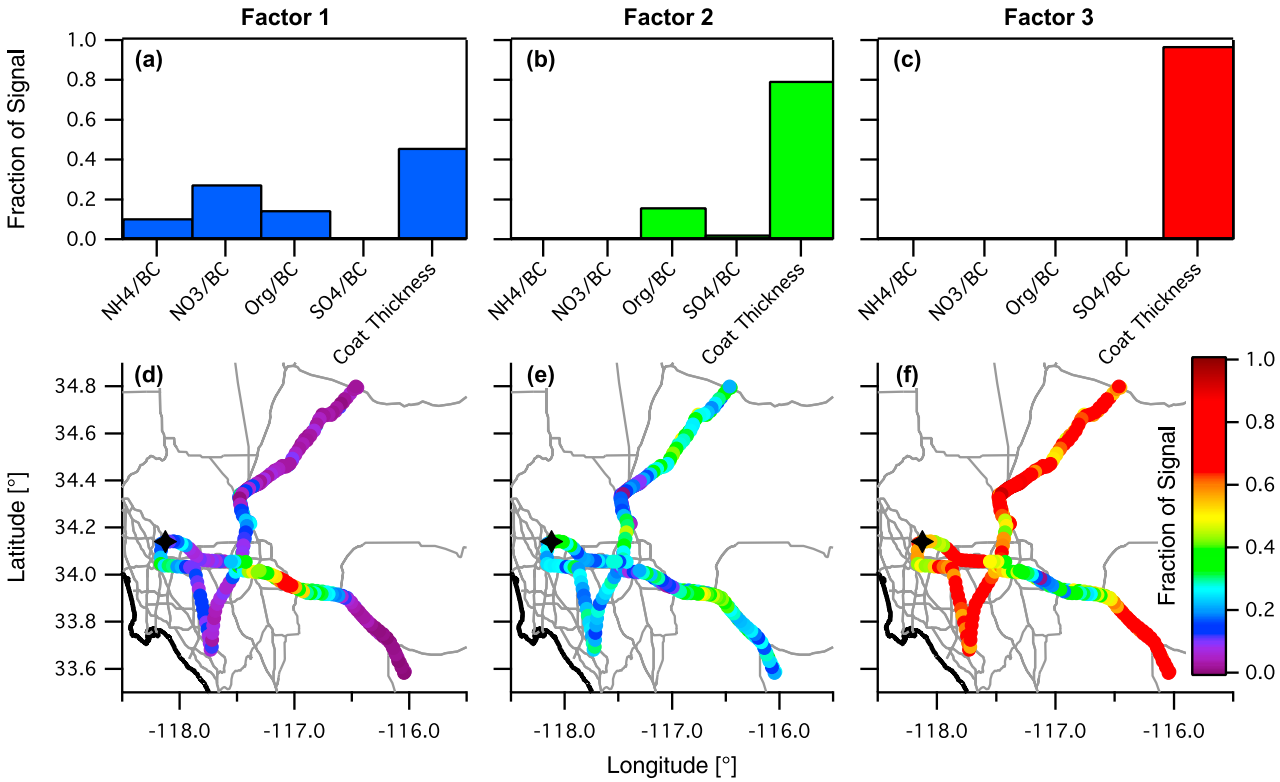

Figure 11. (a, b, and c) Fraction of total signal contributions to each PMF input parameter for each factor of the three-factor PMF model and (d, e, and f) fraction of total signal contributions from each factor to the total signal for the May 25 flight.

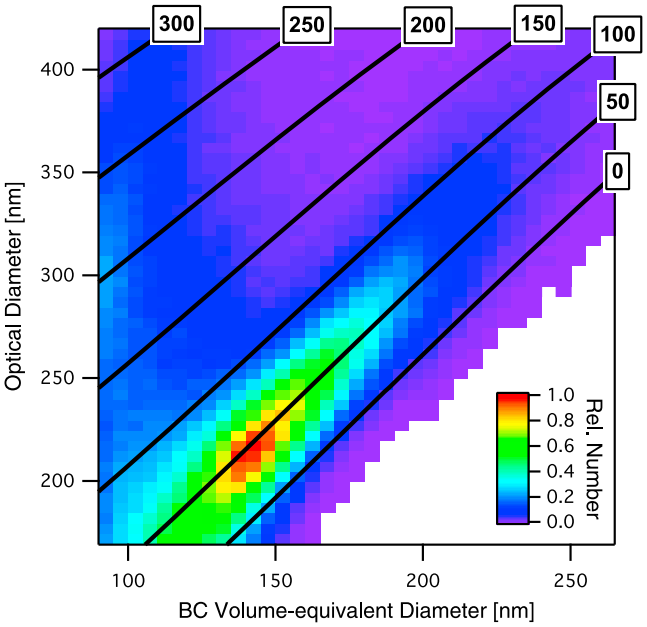

Figure 12. The 2-D histogram of all particles detected in the West LA Basin region as defined in Figure 2. Optical diameter is calculated with a Mie model (assuming a refractive index of 1.5-0.0*i*) fit to the scattering cross-section detected by a LEO fit of these particles' scattering signal. The solid lines denote the results of a core-and-shell Mie model forced with the rBC core diameters on the *x* axis and fit to the equivalent scattering cross-sections on the *y* axis. The numbers denote the shell thickness diameters in nm.

[*Moteki et al.*, 2007]. In the LA Basin, sulfate is a minor constituent of the secondary aerosol relative to nitrate.

[33] In the Banning Outflow region, the overall mass ratio is the smallest, reflecting loss of the volatile species from the aerosol, particularly ammonium nitrate, relative to rBC. For comparison, the Imperial Valley region data are also shown; however, as mentioned above, the timescales over which LA Basin air may mix into this region are unknown. Figures 9c and 9d both show that rBC coating thicknesses increase at the farthest sampling points outside of the LA Basin in both the Banning Outflow and El Cajon Outflow regions. The more noticeable increase in coating thicknesses occurring outside the LA Basin may be due to the timescales necessary for the coatings to grow on rBC. *Moteki et al.* [2007] found that rBC particles become internally mixed on a timescale of about 12 h in urban plumes. Figure 4f shows a sampling location during the May 25 flight in the Banning Outflow region in which the 12-h integrated surface history of the air mass shows a clear link to the eastern LA Basin. The data in Figure 10 show that the water-soluble organics continue to remain high relative to rBC in both the Banning Outflow and Imperial Valley regions and, therefore, likely contribute to any coatings on rBC particles in these regions.

[34] To explain the variation in rBC coating thicknesses, we used Positive Matrix Factorization (PMF) [*Paatero and Tapper*, 1993; *Paterson et al.*, 1999; *Ulbrich et al.*, 2009] with input parameters of mean rBC coating thickness and AMS masses normalized by rBC mass for the May 25 flight. Although Figure 10 shows the presence of two dominant species available as coating materials, nitrate and organics, we used a three-factor PMF model in order to compare with similar previous studies [*Shiraiwa et al.*, 2007, 2008]. The predicted parameters (ammonium/rBC, nitrate/rBC, organics/rBC, sulfate/rBC, and mean rBC coating thickness) by the PMF model agree well with the measured values (R^2 = 0.934, 0.999, 1.000, 0.625, and 1.000, respectively), indicating that the PMF model sufficiently describes the variance in the data. The three factors are shown in Figures 11a–11c. The fraction of signal is the contribution of each parameter to the overall signal and is, thus, weighted by the relative abundances of each parameter over the entire May 25 flight. Thus, the ammonium and sulfate fractions are small, because they have small loadings compared to the nitrate, organics, and mean coating thickness signals. If we look at the average fraction of measured signal accounted for by each factor, Factor 1 (Figure 11a) describes ~90% of the measured nitrate/rBC signal, ~28% of the organics/rBC, but only ~9% of the mean coating thickness. Factor 2 (Figure 11b) describes ~57% of the organics/rBC and ~22% of the mean coating thickness, while Factor 3 (Figure 11c) describes ~15% of the organics/rBC and ~69% of the mean coating thickness. Factors 2 and 3 each only describe ~5% of the nitrate/rBC signal. The cumulative explained fraction of measured signal by the PMF model of nitrate/rBC, organics/rBC, and mean coating thickness are 1.008, 0.999, and 1.000, respectively.

[35] Figures 11d–11f show the spatial pattern of the fraction of total signal contributed by the three factors on the May 25 flight. Factor 1 (Figure 11d) has the largest contribution to the signal in the Banning Pass, coincident with the largest loadings of nitrate measured on this flight. Although the overall explained signal of mean coating thickness for the entire flight is small for this factor, the dominance of the total factor signal in this region means that the coatings are likely nitrate and organics within the Banning Pass. Factor 2 (Figure 11e) has a more highly variable pattern throughout the flight; however, there are noticeable local maxima in several locations, particularly downwind of the Banning Pass in the Banning Outflow region, where this factor makes up ~50% of the total signal. The areas of high Factor 2 signal are characterized by a largely organic rBC coating, consistent with the ammonium nitrate having largely evaporated in this region (Figure 10). Factor 3 (Figure 11f) is dominant, by far, over most of the flight, with the exception of the two areas mentioned above. Because Factor 3 is essentially mean coating thickness by itself (Figure 11c), this factor is, in essence, the residual variation in mean coating thickness not described by Factors 1 and 2. Given its importance over most of the flight, it is clear that the PMF model does not contain enough parameters that vary with mean coating thickness to fully describe, in a physical interpretation, the cause for the variation in coating thickness in most regions. However, in the Banning Pass and Outflow regions, the PMF results support the conclusions from Figure 10 that the available coating materials are largely nitrate and organics, especially in regions where these compounds have relatively high loadings.

4.3. The rBC Mixing State

[36] Figure 12 presents a 2D histogram of all particles measured in the West LA Basin region (see Figure 2) during

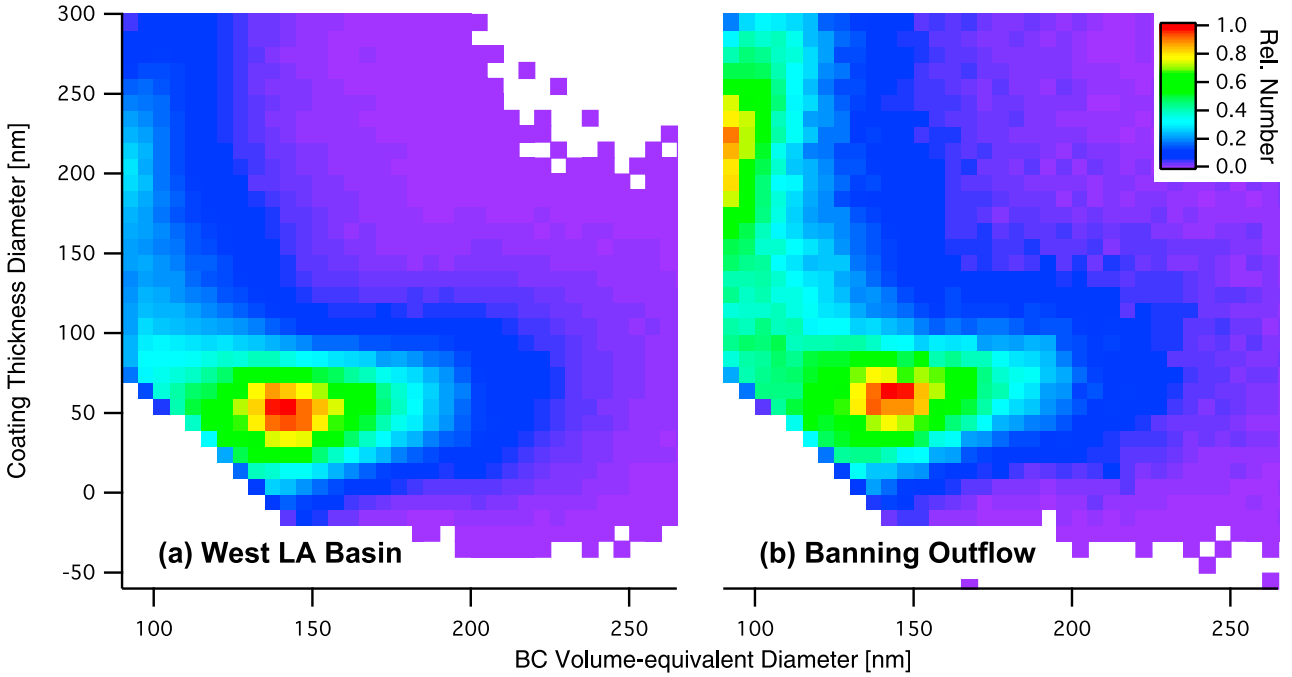

Figure 13. The 2-D histogram of all particles detected in (a) the West LA Basin region and (b) the Banning Outflow region, defined in Figure 2. Coating thickness is derived from a core-and-shell Mie model fit with the detected scattering cross-section by a LEO fit of the scattering signal.

CalNex. rBC core diameters (VED) from 90–260 nm are binned according to their optical diameter (175–410 nm) determined with the LEO method. Optical diameter, calculated using Mie theory assuming that the particle is purely scattering with a refractive index of 1.5-0.0*i*, is used instead of scattering cross-section in this figure for convenience of relating the scattering signal to particle diameter. Given the assumed rBC core sizes of these particles in Figure 12, solid lines representing a core-and-shell Mie model have been overlaid with the shell thickness diameters given in nm. Presented this way, the x- and y-axes limits on Figure 12 are the limits of detection for coated rBC of the Twin Otter SP2. As shown earlier, the MMD peaks below 130 nm for much of the measurements during CalNex, and Figure 12 clearly shows that one cannot determine the mixing state of the majority of these particles unless they have a coating thickness greater than 50 nm in diameter.

[37] Despite these limitations, we can examine how the behavior of coated rBC particles within the detection range of the SP2 change with region. To simplify the presentation of these data, Figure 13a is calculated directly from Figure 12 by re-binning the 2D histogram in terms of the core-and-shell Mie model scattering cross-sections to put the measurement in terms of coating thickness diameter. Figure 13a again shows the limits of detection at small rBC core sizes, as the major mode of coated rBC particles is cut off in the lower-left corner of the plot.

[38] Of particular interest is the evolution of the mixing state of the rBC aerosol as it is transported into the outflow regions. Figures 13a and 13b demonstrate this evolution from the source-rich area of the western LA Basin to the more aged Banning Outflow region. Figure 13 clearly shows that a second mode of particles at small rBC VED's but with thick (≥150 nm) coatings become more important relative to the main mode of more thinly-coated, larger rBC in the outflows. In the source-rich region of the western LA Basin, this second mode is barely visible as compared to the main mode of thinly coated rBC, indicating a dominance of thinly coated rBC particles, largely outside the detection range of the SP2.

4.4. Variability of rBC Levels With Altitude

[39] Figure 14a shows the 1-min resolution rBC mass concentration for all research flights as a function of altitude with single soundings presented in Figures 14b and 14c. In general, rBC mass concentration decreases with altitude, with the smallest concentrations measured in the free troposphere. In contrast, the mean coating thickness increases with altitude, with a dramatic increase above the inversion layer. The trend of lower rBC concentrations with increasing coating thickness is also shown in Figure 6. That the more thickly coated rBC particles lie in the free troposphere is consistent with a more aged aerosol, on which secondary species have condensed. A dramatic shift in MMD occurs above the inversion layer, indicating the rBC cores themselves are larger in the free troposphere. The characteristic time for coagulation by rBC-containing particles only in the free troposphere is about 82 days, but that of all particles in this region is about 7 days (using a coagulation coefficient $K = 6.41 \times 10^{-9}$ cm^3 s^{-1} calculated from the measurements) [*Seinfeld and Pandis*, 2006]. While this seems excessively long for the rBC particles, it is likely that rBC concentrations were much higher at their source, meaning

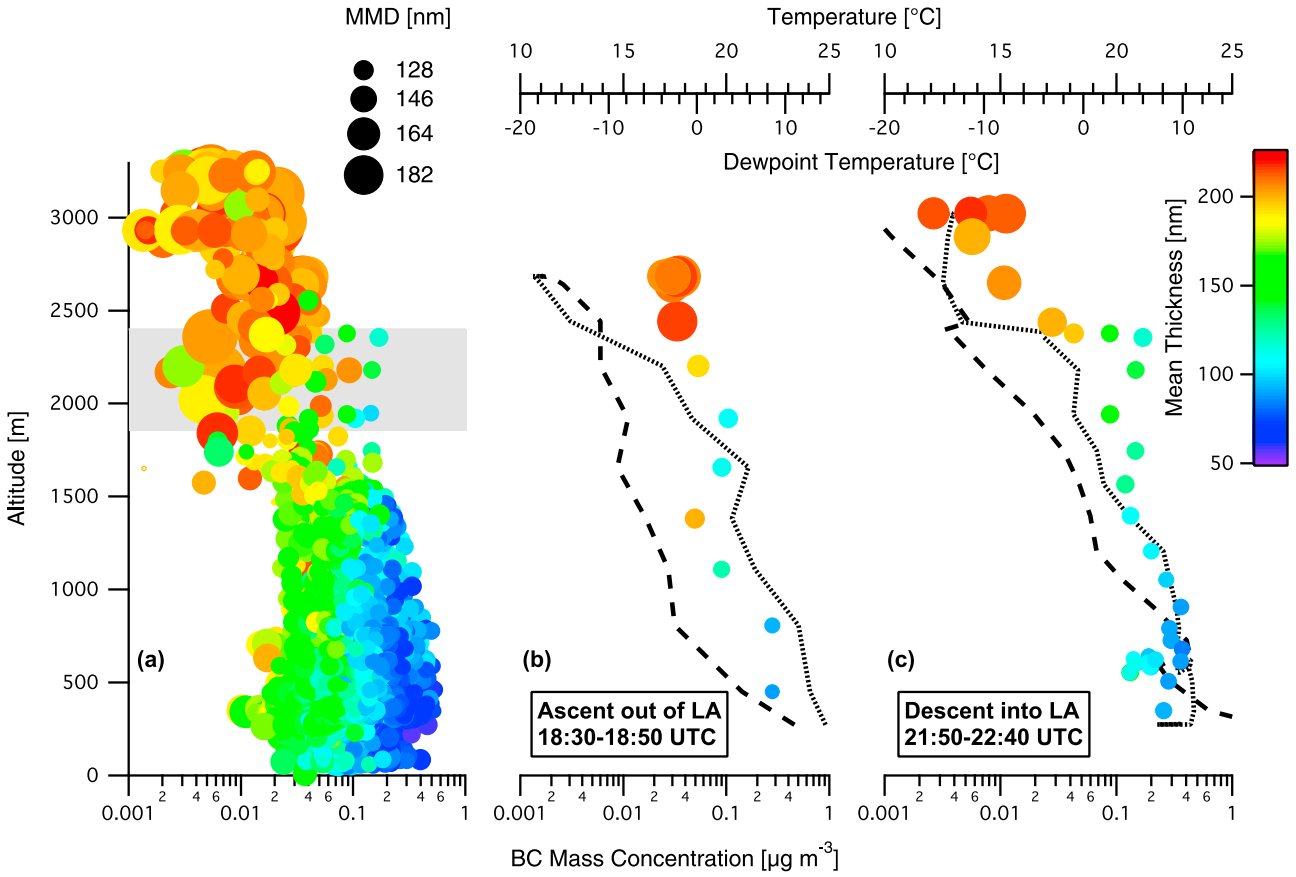

Figure 14. Vertical distribution of (a) all SP2 measurements, (b) ascent out of LA on May 20, and (c) descent into LA 3 h later. Each marker is a 1-min average data point indicating rBC mass concentration (x axis), mean coating thickness on rBC particles (marker color), and MMD (marker size). The gray shaded region in Figure 14a denotes the range of inversion layer altitudes observed during CalNex. The dashed lines in Figures 14b and 14c are the ambient temperature profiles and the dotted lines are the dew point temperature profiles.

coagulation would have proceeded much faster initially before being transported above the inversion. Another possible explanation is that the rBC above the inversion layer is from a different combustion source (biogenic vs. anthropogenic) than for the fresh rBC particles in the Basin, which may have caused larger rBC core sizes to begin with [*Schwarz et al.*, 2008a].

[40] Figures 14b and 14c show single soundings out of and back into the LA Basin on May 20. These soundings are for the same time periods as those presented in Figure 5 of *Duong et al.* [2011]. The ascent took place before noon local time on the east side of the LA Basin near the El Cajon Pass, and the temperature profile indicates the presence of a weak inversion layer ($\Delta T = \sim 0.5°C$ at $\sim$1800 m) and a layer of elevated rBC levels (an increase of ~ 0.05 $\mu g\ m^{-3}$) around the same level. The decrease in dew point temperature (6.4°C) over this same layer is more dramatic and continues to decrease above this layer, indicating a much drier air mass aloft. Three hours later, on the descent into the LA Basin, again near the El Cajon Pass, rBC levels below the inversion layer are higher overall, especially near the base of the inversion layer ($\Delta T = \sim 1.6°C$ at $\sim$2400 m). Again, the dew point temperature profile shows a sharp decrease (9.3°C) indicating a much drier air mass aloft. Although *Raga et al.* [2001] argue that the presence of an absorbing aerosol layer just above the temperature inversion helps to strengthen the inversion layer near Mexico City, we do not have enough soundings at sufficiently high resolution to evaluate this for the LA Basin. In fact, the data show that the rBC mass concentrations on this flight are higher below the inversion, especially later in the afternoon. Figures 14b and 14c also show the presence of rBC layers with different mean coating thicknesses. On the ascent out of the LA Basin, there is a layer of rBC at $\sim$1400 m altitude with a mean coating thickness of $\sim$200 nm surrounded above and below by rBC layers with mean coating thicknesses of $\sim$115 nm. On the descent into the LA Basin later in the day, just below the inversion layer, at $\sim$2350 m altitude, the local maxima in rBC mass concentration (an increase of ~ 0.08 $\mu g\ m^{-3}$) coincides with a mean coating thickness of $\sim$115 nm with surrounding layers >160 nm in coating thickness. The descent also records the presence of a second inversion ($\Delta T = \sim 2.4°C$) much closer to the surface ($\sim$600 m altitude) in which a layer of rBC with mean

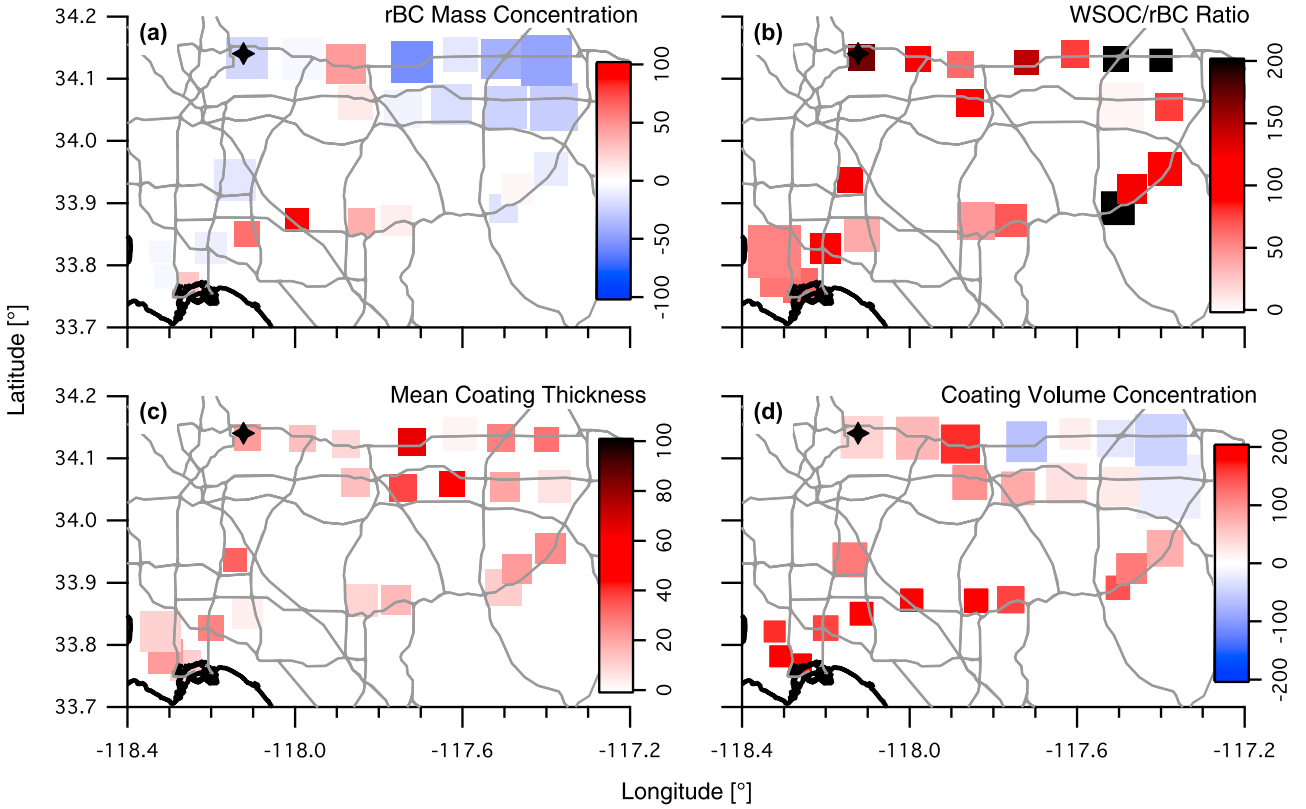

Figure 15. Percent change between Friday, May 14 and Saturday, May 15 measurements displayed as percent change from the May 14 values (marker color) for: (a) rBC mass concentration, (b) WSOC/rBC ratio, (c) mean coating thickness, and (d) coating volume concentration. The SP2 measurements are averaged over a grid spacing of 0.12° longitude by 0.1° latitude. The size of the markers in each plot is proportional to the May 14 measurement value. The stars denote the CalNex LA ground site at Caltech.

coating thickness ~150 nm is surrounded by layers with coating thicknesses of ~105 nm. The complicated vertical structure in Figures 14b and 14c is likely the result of the "mountain-chimney effect" described by *Lu and Turco* [1994, 1995]. In both soundings, the rBC just above the inversion layer is dramatically different than below; the rBC is much more thickly coated and the mass median diameters are much larger.

4.5. Case Study: "Weekend Effect" on rBC Aerosol

[41] Ozone levels in the LA Basin are subject to the well-documented weekday-weekend effect [e.g., *Marr and Harley*, 2002; *Pollack et al.*, 2012]. This so-called "weekend effect" is a result of the dramatically reduced amount of heavy-duty truck traffic (diesel truck emissions decrease by 60–80%), as reflected primarily in NO_x levels [*Harley et al.*, 2005].

[42] To examine the possible effects on rBC in the LA Basin as a result of the weekend effect, Figure 15 presents the percent change of several measurements from Friday, May 14 to Saturday, May 15. We define the percent change referenced to the measurements from May 14; thus, positive values denote measurements that are higher on the weekend flight of May 15. The size of the markers is proportional to the measured values on May 14, revealing the weekday pattern of larger values in the Basin. Figure 15a shows rBC mass concentration changes in the Basin (see Figures 8f and 8g for actual measurements). By flight average, there is virtually no change in rBC levels from May 14 to 15 (+0.01%), but there are regions within the Basin of increase and decrease. Figure 15b shows change in the WSOC/rBC ratio, which is indicative of secondary organic aerosol (SOA) formation, increasing everywhere in the Basin by a large percent. This observation is consistent with previous observations that the highest levels of SOA formation in the LA Basin occur on weekends [*Turpin and Huntzicker*, 1991, 1995]. Figure 15c shows that mean coating thicknesses also increase everywhere on May 15 throughout the LA Basin. Finally, Figure 15d shows that in the far northeast corner of the LA Basin the coating volume concentration is smaller on May 15, in contrast to the rest of the Basin which has more coating volume on this particular Saturday. While this may seem to conflict with Figure 15c, note that mean coating thickness is a particle-by-particle average, which gives the mean state of single rBC particles, whereas coating volume concentration is a bulk measurement that reflects total number concentration as well as average coating thickness. Thus, on Friday, May 14, there were more particles in the LA Basin, and thus more total coating volume on rBC in the northeast corner of the Basin, where pollution accumulates,

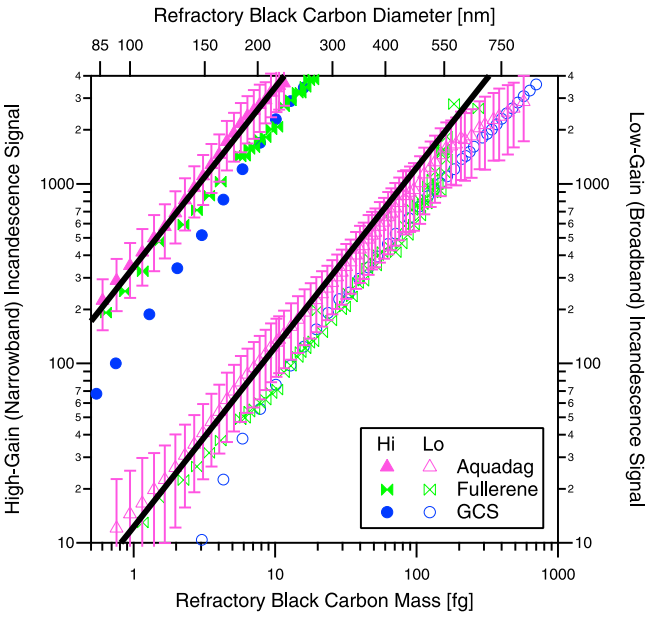

Figure A1. Calibration data for the high-gain (upper-left trace) and low-gain (lower-right trace) incandescence channels. The rBC mass (bottom x axis) is calculated from the selected mobility diameter with mobility density for Aquadag and Fullerene from *Gysel et al.* [2011] and density = 1.4 g cm^{-3} for glassy carbon spheres (GCS). rBC diameter (top x axis) is volume-equivalent diameter (VED) calculated as for ambient particles, assuming a spherical particle with a density = 1.8 g cm^{-3}. The solid line is the calibration curve used in this study, calculated from the Aquadag data only.

despite the fact that per rBC particle, there was a thinner coating of material.

5. Summary

[43] The present work reports rBC measurements during May 2010 as part of the CalNex 2010 field experiment in California. The measurements were carried out onboard the CIRPAS Twin Otter aircraft during 18 research flights, using the Single Particle Soot Photometer. The dominant feature controlling the regional variability of rBC aerosol in the LA Basin is the daytime southwesterly sea breeze. The sea breeze advects the fresh LA plume inland, where mountain ranges and a shallow inversion layer collect the pollution before exiting the Basin through two narrow mountain passes. While rBC mass concentrations remain fairly uniform west-to-east within the Basin, there is clear growth of secondary organics and ammonium nitrate as the LA plume is advected eastward in the Basin. This secondary growth coincides with an increase in the coating thickness on rBC particles from west to east. In the outflow regions, the volatile ammonium nitrate largely evaporates, leaving WSOC as the most abundant secondary material available to contribute to the growing mean rBC coating thicknesses. Detailed analysis of the rBC mixing state reveals two modes of coated particles, one with an rBC VED ~145 nm with a coating that grows from ~50 nm to ~70 nm from the western LA Basin to the Banning Outflow region and one with an rBC VED ~90 nm, on the edge of the SP2 detection range, with a coating that grows from <100 nm (out of detection range) to >200 nm. In general, rBC mass concentrations decrease with altitude, while the coating thickness increases dramatically above the inversion layer, consistent with a more aged aerosol in the free troposphere. The "weekend effect" on rBC resulted in more thickly coated rBC particles on a Saturday versus the preceding Friday everywhere in the LA Basin, coinciding with higher WSOC/BC ratios, indicating more secondary formation of aerosol on Saturday.

Appendix A: Calibration of the SP2

A1. The rBC Mass Calibration

[44] The SP2 has two incandescence channels, a broadband (λ = 350–800 nm) and a narrowband (λ = 630–800 nm) channel. The Twin Otter SP2 was additionally configured such that the broadband incandescence channel was set to a higher gain setting than the narrowband channel, to increase the total range of detectable refractory black carbon mass. Figure A1 presents the incandescence calibration for the two channels, showing the clear overlap in signal ranges and deviation of the signal from the linear fit at larger particle masses. A comparison is made to other rBC aerosol standards, Fullerene soot (stock #40971, lot #G25N20, Alfa Aesar, Ward Hill, MA, USA) and glassy carbon spheres (GCS, Type II, stock #38008, lot #C14K07, Alfa Aesar). The mass of generated Fullerene particles is calculated using the relation from *Gysel et al.* [2011]; however, we note that our batch of Fullerene is different from that used in their study. GCS mobility diameter is converted to mass using the manufacturer-reported density of 1.42 g cm^{-3}. The Fullerene and GCS calibration slopes are both ~37% larger than the Aquadag slope, meaning that these calibrations would yield larger rBC masses. When more data becomes available relating these three rBC standards to ambient rBC in the LA Basin, corrections to the calibration can be made.

[45] The SP2 incandescence channels were calibrated with Aquadag by nebulizing a solution of Aquadag and milliQ water through a differential mobility analyzer (DMA, TSI Model 3081) used to classify the mobility of the generated particles. The mass of those particles was calculated from the mobility diameter using the relation from *Gysel et al.* [2011], who showed that Aquadag mobility density is independent of production batch and specific aerosol generation procedures. We have chosen to use Aquadag as our calibration standard because of this published density and because the different production lots of Aquadag have been distributed to most SP2 users by DMT; thus, providing a means to inter-relate the many SP2 instruments. Recent work by *Laborde et al.* [2012] instead recommend the use of Fullerene soot, as has been recommended previously [*Moteki and Kondo*, 2010]. However, the mobility density of Fullerene soot is not consistent across different production lots and may vary by up to 14% between specific batches [*Laborde et al.*, 2012]. For this study, we did not have access to a particle mass analyzer and, therefore, could not verify the mobility density of our batch of Fullerene.

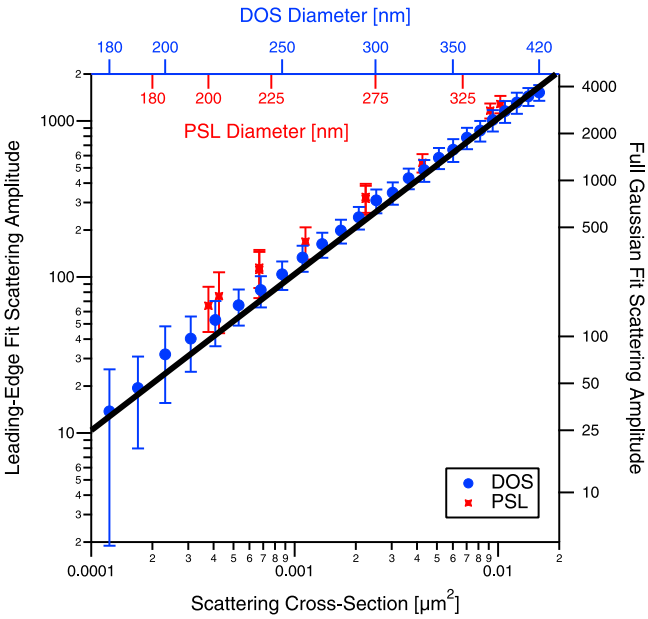

Figure A2. PSL and DOS scattering calibration data. Each data point is the median of about 10,000 particles, and the error bars indicate one standard deviation. For reference, both the full Gaussian and the leading-edge only fits are shown, but operationally, only the leading edge fits are used to determine an optical diameter.

[46] It has been previously shown that the incandescence response of the SP2 is linear up to particle masses of 10 fg and independent of particle shape or mixing state [*Moteki and Kondo*, 2007, 2010; *Slowik et al.*, 2007]. We have found a linear response over a slightly larger range, up to at least a 50 fg particle (see Figure A1), before surface area effects lead to a power law dependence in the signal. The coefficients of determination (R^2 = 0.993, 0.996, and 0.997 for Aquadag, Fullerene, and GCS, respectively) clearly demonstrate the linearity in the response of the SP2 to rBC mass. We have chosen to fit both incandescence channels with a linear function and note that errors will be greatest at the extreme large end of the rBC mass spectrum, where few particles were detected in this study. The detection limit of the high-gain broadband incandescence channel was 0.48–11.1 fg rBC per particle (80–227 nm VED) and of the low-gain narrowband incandescence channel was 3.66–317 fg rBC per particle (157–696 nm VED).

A2. Scattering Calibration

[47] The SP2 has two scattering channels, a high-gain and a low-gain channel, which are filtered to detect scattered light at λ = 1064 nm. The Twin Otter SP2 was configured with a split-detector on the high-gain scatter channel, which is used to obtain particle position information for use in a leading-edge only (LEO) fit of the scattering data on the low-gain channel [*Gao et al.*, 2007]. The scattering channels were calibrated with both dioctyl sebecate (DOS, refractive index = 1.45-0.0i) and polystyrene latex spheres (PSL, refractive index = 1.59-0.0*i*) size-selected by a DMA. Figure A2 shows the results of the calibration for a full Gaussian fit to the scattering signal and for the LEO fits to the scattering signal, detailed below. A Mie scattering model is used to relate diameter and refractive index to the scattering cross-section. In Figure A2, each data point represents the median of a sample of about 10,000 particles. The error bars are one standard deviation of the LEO fit amplitude, indicative of the spread in the data for each size. The linear fit was found by forcing a zero intercept, but very little change in slope occurs if this criterion is relaxed. The data used to generate the linear fit were the DOS data only. Both DOS and PSL calibration curves demonstrate the linearity of the scattering response of the SP2 to scattering cross-section (R^2 = 0.996 and 0.999, respectively). Uncertainty in the full Gaussian fit amplitude is ~14%.

A3. LEO Fitting

[48] We desire to use only the leading-edge of the scattering signal so that coated rBC particles, which have a scattering signal that begins as a Gaussian shape but then is perturbed as the coating evaporates, may be sized according to their full, unperturbed diameter. We have chosen the criterion for determining the last point in the leading-edge signal consistent with *Gao et al.* [2007]; that is, an amplification factor of 30, which means signals up to the point where the signal is 3.33% of the maximum observed signal for that particle are used in the LEO fit.

[49] In addition to using only a limited portion of the scattering signal for each particle, we simplify the Gaussian fit based on calibration results. The Gaussian-shaped scatter signal, S, as a function of time, t, on the low-gain scatter channel is written as

$$S(t) = a\exp\left[-4\ln 2\left(\frac{t-b}{c}\right)^2\right] + d \qquad \text{(A1)}$$

where a is the height of the peak, b is the position of the center of the peak, c is the full width at half maximum, and d is the baseline or offset. Owing to the constant flow rate and width of the laser in the instrument, purely scattering particles of all sizes exhibit the same full width at half maximum (c) and peak position (b) relative to the zero-crossing of the split-detector (labeled as "Position Time" on Figure 5) [*Gao et al.*, 2007]. Thus, equation (A1) can be simplified to

$$S(t) = aX(t) + d \qquad \text{(A2)}$$

where $X = \exp\left(-4\ln 2\left(\frac{t-b}{c}\right)^2\right)$ can be calculated directly from calibration data and S, a, and d are defined above. In fitting equation (A2), we do not restrict the value of d, the signal baseline, but keep it as a free parameter and compare the fitted d to the baseline value estimated as the minimum average of the first or last 20 signal data points on the single-particle time trace (Figure 5). This comparison ensures that the fit to the scattering data yields realistic values for a. Due to fluctuations in sample flow and laser profile, LEO fitting increases uncertainty in the retrieved scattering amplitude to ~22%.

[50] To validate the LEO method of fitting, we compared the full Gaussian fit amplitude to the leading-edge fits for the

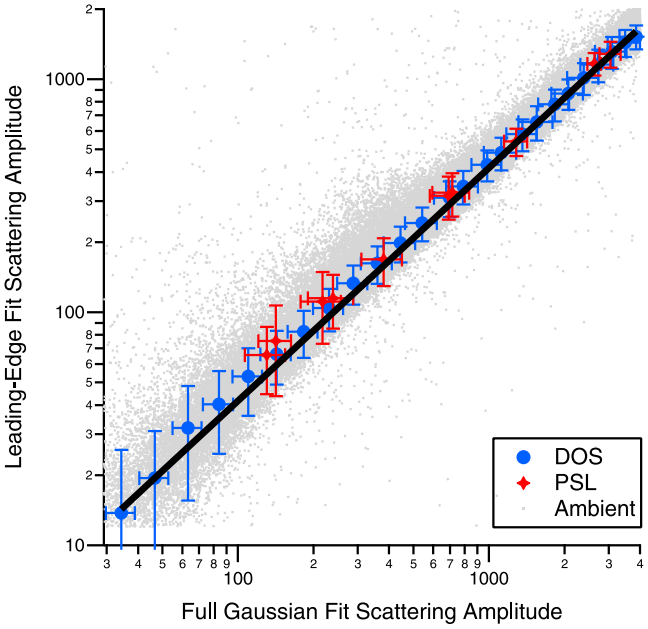

Figure A3. Comparison of the leading-edge only (LEO) fit amplitudes to the full Gaussian fit amplitudes for purely scattering particles. DOS ($R^2 = 0.998$) and PSL ($R^2 = 0.999$) calibration data are shown, as well as purely scattering ambient particle data from one of the flights during CalNex.

DOS and PSL calibration data as well as for a subset of purely scattering particle data from several of the research flights. The results are given in Figure A3. For clarity, the fits from a segment of only one of the flights is shown, but all flights gave similar results. Although the slope between the two methods is not ideally unity, the linearity of the plot (R^2 = 0.998 and 0.999 for DOS and PSL, respectively) validates this as an effective method for sizing particles.

[51] **Acknowledgments.** This work was supported by NOAA grant NA09OAR4310128. The authors wish to thank Greg Kok at DMT and Anne Perring and Joshua (Shuka) Schwarz at NOAA for their guidance on data analysis and calibration. We also acknowledge the entire CIRPAS crew for their professionalism and assistance during the campaign.

References

Andreae, M., O. Schmid, H. Yang, D. Chand, J. Zhen Yu, L. Zeng, and Y. Zhang (2008), Optical properties and chemical composition of the atmospheric aerosol in urban Guangzhou, China, *Atmos. Environ.*, *42*, 6335–6350, doi:10.1016/j.atmosenv.2008.01.030.

Babu, S. S., S. K. Satheesh, and K. K. Moorthy (2002), Aerosol radiative forcing due to enhanced black carbon at an urban site in India, *Geophys. Res. Lett.*, *29*(18), 1880, doi:10.1029/2002GL015826.

Bauer, S. E., S. Menon, D. Koch, T. C. Bond, and K. Tsigaridis (2010), A global modeling study on carbonaceous aerosol microphysical characteristics and radiative effects, *Atmos. Chem. Phys.*, *10*, 7439–7456, doi:10.5194/acp-10-7439-2010.

Baumgardner, D., G. L. Kok, and G. Raga (2004), Warming of the Arctic lower stratosphere by light absorbing particles, *Geophys. Res. Lett.*, *31*, L06117, doi:10.1029/2003GL018883.

Baumgardner, D., G. L. Kok, and G. B. Raga (2007), On the diurnal variability of particle properties related to light absorbing carbon in Mexico City, *Atmos. Chem. Phys.*, *7*, 2517–2526, doi:10.5194/acp-7-2517-2007.

Binkowski, F. S., and S. J. Roselle (2003), Models-3 Community Multiscale Air Quality (CMAQ) model aerosol component: 1. Model description, *J. Geophys. Res.*, *108*(D6), 4183, doi:10.1029/2001JD001409.

Blumenthal, D., W. White, and T. Smith (1978), Anatomy of a Los Angeles smog episode: Pollutant transport in the daytime sea breeze regime, *Atmos. Environ.*, *12*(4), 893–907, doi:10.1016/0004-6981(78)90028-8.

Bohren, C. F., and D. R. Huffman (1998), *Absorption and Scattering of Light by Small Particles*, John Wiley, New York.

Bond, T. C. (2007), Can warming particles enter global climate discussions?, *Environ. Res. Lett.*, *2*(4), 045030, doi:10.1088/1748-9326/2/4/045030.

Bond, T. C., and R. W. Bergstrom (2006), Light absorption by carbonaceous particles: An investigative review, *Aerosol Sci. Technol.*, *40*(1), 27–67, doi:10.1080/02786820500421521.

Bond, T. C., G. Habib, and R. W. Bergstrom (2006), Limitations in the enhancement of visible light absorption due to mixing state, *J. Geophys. Res.*, *111*, D20211, doi:10.1029/2006JD007315.

Brioude, J., et al. (2009), Effect of biomass burning on marine stratocumulus clouds off the California coast, *Atmos. Chem. Phys.*, *9*, 8841–8856, doi:10.5194/acp-9-8841-2009.

Brunciak, P. A., J. Dachs, T. P. Franz, C. L. Gigliotti, E. D. Nelson, B. J. Turpin, and S. J. Eisenreich (2001), Polychlorinated biphenyls and particulate organic/elemental carbon in the atmosphere of Chesapeake Bay, USA, *Atmos. Environ.*, *35*(32), 5663–5677, doi:10.1016/S1352-2310(01)00222-9.

Chazette, P., and C. Liousse (2001), A case study of optical and chemical ground apportionment for urban aerosols in Thessaloniki, *Atmos. Environ.*, *35*(14), 2497–2506, doi:10.1016/S1352-2310(00)00425-8.

Chow, J. C., J. G. Watson, E. M. Fujita, Z. Lu, D. R. Lawson, and L. L. Ashbaugh (1994), Temporal and spatial variations of $PM_{2.5}$ and PM_{10} aerosol in the Southern California Air Quality Study, *Atmos. Environ.*, *28*(12), 2061–2080, doi:10.1016/1352-2310(94)90474-X.

Chow, J. C., J. G. Watson, Z. Lu, D. H. Lowenthal, C. A. Frazier, P. A. Solomon, R. H. Thuillier, and K. Magliano (1996), Descriptive analysis of $PM_{2.5}$ and PM_{10} at regionally representative locations during SJVAQS/AUSPEX, *Atmos. Environ.*, *30*(12), 2079–2112, doi:10.1016/1352-2310(95)00402-5.

Chung, S. H., and J. H. Seinfeld (2005), Climate response of direct radiative forcing of anthropogenic black carbon, *J. Geophys. Res.*, *110*, D11102, doi:10.1029/2004JD005441.

Clarke, A. D., et al. (2004), Size distributions and mixtures of dust and black carbon aerosol in Asian outflow: Physiochemistry and optical properties, *J. Geophys. Res.*, *109*, D15S09, doi:10.1029/2003JD004378.

Collins, D. R., H. H. Jonsson, H. Liao, R. C. Flagan, J. H. Seinfeld, K. J. Noone, and S. Hering (2000), Airborne analysis of the Los Angeles aerosol, *Atmos. Environ.*, *34*(24), 4155–4173, doi:10.1016/S1352-2310(00)00225-9.

Cubison, M. J., B. Ervens, G. Feingold, K. S. Docherty, I. M. Ulbrich, L. Shields, K. Prather, S. Hering, and J. L. Jimenez (2008), The influence of chemical composition and mixing state of Los Angeles urban aerosol on CCN number and cloud properties, *Atmos. Chem. Phys.*, *8*, 5649–5667, doi:10.5194/acp-8-5649-2008.

de Foy, B., J. Varela, L. Molina, and M. Molina (2006), Rapid ventilation of the Mexico City basin and regional fate of the urban plume, *Atmos. Chem. Phys.*, *6*, 2321–2335, doi:10.5194/acp-6-2321-2006.

Del Delumyea, R., and A. Kalivretenos (1987), Elemental carbon and lead content of fine particles from American and French cities of comparable size and industry, 1985, *Atmos. Environ.*, *21*(7), 1643–1647, doi:10.1016/0004-6981(87)90325-8.

Dentener, F., et al. (2006), Emissions of primary aerosol and precursor gases in the years 2000 and 1750 prescribed data-sets for AeroCom, *Atmos. Chem. Phys.*, *6*, 4321–4344, doi:10.5194/acp-6-4321-2006.

Didyk, B. M., B. R. T. Simoneit, L. A. Pezoa, M. L. Riveros, and A. A. Flores (2000), Urban aerosol particles of Santiago, Chile: Organic content and molecular characterization, *Atmos. Environ.*, *34*(8), 1167–1179, doi:10.1016/S1352-2310(99)00403-3.

Ding, A., et al. (2009), Transport of north China air pollution by midlatitude cyclones: Case study of aircraft measurements in summer 2007, *J. Geophys. Res.*, *114*, D08304, doi:10.1029/2008JD011023.

Docherty, K. S., et al. (2008), Apportionment of primary and secondary organic aerosols in Southern California during the 2005 Study of Organic Aerosols in Riverside (SOAR-1), *Environ. Sci. Technol.*, *42*(20), 7655–7662, doi:10.1021/es8008166.

Drewnick, F., et al. (2005), A new time-of-flight aerosol mass spectrometer (TOF-AMS)–Instrument description and first field deployment, *Aerosol Sci. Technol.*, *39*(7), 637–658, doi:10.1080/02786820500182040.

Duong, H. T., et al. (2011), Water-soluble organic aerosol in the Los Angeles Basin and outflow regions: Airborne and ground measurements during the 2010 CalNex field campaign, *J. Geophys. Res.*, *116*, D00V04, doi:10.1029/2011JD016674.

Edinger, J. G. (1959), Changes in the depth of the marine layer over the Los Angeles Basin, *J. Meteorol.*, *16*, 219–226, doi:10.1175/1520-0469(1959)016<0219:CITDOT>2.0.CO;2.

Ensor, D. S., R. J. Charlson, N. C. Alhquist, K. T. Whitby, R. B. Husar, and B. Y. H. Liu (1972), Multiwavelength nephelometer measurements in

Los Angeles smog aerosol. I. Comparison of calculated and measured light scattering, *J. Colloid Interface Sci.*, *39*(1), 242–251, doi:10.1016/0021-9797(72)90159-2.

Fine, P. M., S. Shen, and C. Sioutas (2004), Inferring the sources of fine and ultrafine particulate matter at downwind receptor sites in the Los Angeles Basin using multiple continuous measurements, *Aerosol Sci. Technol.*, *38*(S1), 182–195, doi:10.1080/02786820390229499.

Fuller, K. A., W. C. Malm, and S. M. Kreidenweis (1999), Effects of mixing on extinction by carbonaceous particles, *J. Geophys. Res.*, *104*(D13), 15,941–15,954, doi:10.1029/1998JD100069.

Gao, R. S., et al. (2007), A novel method for estimating light-scattering properties of soot aerosols using a modified single-particle soot photometer, *Aerosol Sci. Technol.*, *41*(2), 125–135, doi:10.1080/02786820601118398.

Gray, H. A., G. R. Cass, J. J. Huntzicker, E. K. Heyerdahl, and J. A. Rau (1986), Characteristics of atmospheric organic and elemental carbon particle concentrations in Los Angeles, *Environ. Sci. Technol.*, *20*(6), 580–589, doi:10.1021/es00148a006.

Gysel, M., M. Laborde, J. S. Olfert, R. Subramanian, and A. J. Gröhn (2011), Effective density of Aquadag and fullerene soot black carbon reference materials used for SP2 calibration, *Atmos. Meas. Tech.*, *4*, 2851–2858, doi:10.5194/amt-4-2851-2011.

Hansen, A. D. A., V. N. Kapustin, V. M. Kopeikin, D. A. Gillette, and B. A. Bodhaine (1993), Optical absorption by aerosol black carbon and dust in a desert region of Central Asia, *Atmos. Environ., Part A*, *27*(16), 2527–2531, doi:10.1016/0960-1686(93)90025-T.

Harley, R. A., L. C. Marr, J. K. Lehner, and S. N. Giddings (2005), Changes in motor vehicle emissions on diurnal to decadal time scales and effects on atmospheric composition, *Environ. Sci. Technol.*, *39*(14), 5356–5362, doi:10.1021/es048172+.

He, K. B., F. M. Yang, Y. L. Ma, Q. Zhang, X. H. Yao, C. K. Chan, S. Cadle, T. Chan, and P. Mulawa (2001), The characteristics of $PM_{2.5}$ in Beijing, China, *Atmos. Environ.*, *35*(29), 4959–4970, doi:10.1016/S1352-2310(01)00301-6.

Healy, R. M., et al. (2012), Sources and mixing state of size-resolved elemental carbon particles in a European megacity: Paris, *Atmos. Chem. Phys.*, *12*, 1681–1700, doi:10.5194/acp-12-1681-2012.

Hegg, D., D. Covert, H. Jonsson, and P. Covert (2005), Determination of the transmission efficiency of an aircraft aerosol inlet, *Aerosol Sci. Technol.*, *39*(10), 966–971, doi:10.1080/02786820500377814.

Hitzenberger, R., and S. Tohno (2001), Comparison of black carbon (BC) aerosols in two urban areas—Concentrations and size distributions, *Atmos. Environ.*, *35*(12), 2153–2167, doi:10.1016/S1352-2310(00)00480-5.

Huang, X.-F., et al. (2011), Black carbon measurements in the Pearl River Delta region of China, *J. Geophys. Res.*, *116*, D12208, doi:10.1029/2010JD014933.

Jacobson, M. Z. (1997), Development and application of a new air pollution modeling system—Part III. Aerosol-phase simulations, *Atmos. Environ.*, *31*(4), 587–608, doi:10.1016/S1352-2310(96)00201-4.

Jacobson, M. Z. (2002), Control of fossil-fuel particulate black carbon and organic matter, possibly the most effective method of slowing global warming, *J. Geophys. Res.*, *107*(D19), 4410, doi:10.1029/2001JD001376.

Jacobson, M. Z. (2006), Effects of externally-through-internally-mixed soot inclusions within clouds and precipitation on global climate, *J. Phys. Chem. A*, *110*(21), 6860–6873, doi:10.1021/jp056391r.

Jaffe, D., et al. (1999), Transport of Asian air pollution to North America, *Geophys. Res. Lett.*, *26*(6), 711–714, doi:10.1029/1999GL900100.

Janssen, N. A. H., D. F. M. Van Mansom, K. Van Der Jagt, H. Harssema, and G. Hoek (1997), Mass concentration and elemental composition of airborne particulate matter at street and background locations, *Atmos. Environ.*, *31*(8), 1185–1193, doi:10.1016/S1352-2310(96)00291-9.

Jayne, J. T., D. C. Leard, X. Zhang, P. Davidovits, K. A. Smith, C. E. Kolb, and D. R. Worsnop (2000), Development of an aerosol mass spectrometer for size and composition analysis of submicron particles, *Aerosol Sci. Technol.*, *33*(1–2), 49–70, doi:10.1080/027868200410840.

Johnson, K. S., B. Zuberi, L. T. Molina, M. J. Molina, M. J. Iedema, J. P. Cowin, D. J. Gaspar, C. Wang, and A. Laskin (2005), Processing of soot in an urban environment: Case study from the Mexico City metropolitan area, *Atmos. Chem. Phys.*, *5*, 3033–3043, doi:10.5194/acp-5-3033-2005.

Jones, G. S., N. Christidis, and P. A. Stott (2011), Detecting the influence of fossil fuel and bio-fuel black carbon aerosols on near surface temperature changes, *Atmos. Chem. Phys.*, *11*, 799–816, doi:10.5194/acp-11-799-2011.

Kadowaki, S. (1990), Characterization of carbonaceous aerosols in the Nagoya urban area. 1. Elemental and organic carbon concentrations and the origin of organic aerosols, *Environ. Sci. Technol.*, *24*(5), 741–744, doi:10.1021/es00075a020.

Kim, B. M., S. Teffera, and M. D. Zeldin (2000), Characterization of $PM_{2.5}$ and PM_{10} in the South Coast Air Basin of Southern California: Part 1–Spatial variations, *J. Air Waste Manage. Assoc.*, *50*(12), 2034–2044.

Kim, Y. P., K.-C. Moon, J. H. Lee, and N. J. Baik (1999), Concentrations of carbonaceous species in particles at Seoul and Cheju in Korea, *Atmos. Environ.*, *33*(17), 2751–2758, doi:10.1016/S1352-2310(98)00313-6.

Laborde, M., P. Mertes, P. Zieger, J. Dommen, U. Baltensperger, and M. Gysel (2012), Sensitivity of the single particle soot photometer to different black carbon types, *Atmos. Meas. Tech. Discuss.*, *5*, 663–690, doi:10.5194/amtd-5-663-2012.

Lack, D. A., and C. D. Cappa (2010), Impact of brown and clear carbon on light absorption enhancement, single scatter albedo and absorption wavelength dependence of black carbon, *Atmos. Chem. Phys.*, *10*, 4207–4220, doi:10.5194/acp-10-4207-2010.

Langford, A. O., J. Brioude, O. R. Cooper, C. J. Senff, R. J. Alvarez II, R. M. Hardesty, B. J. Johnson, and S. J. Oltmans (2012), Stratospheric influence on surface ozone in the Los Angeles area during late spring and early summer of 2010, *J. Geophys. Res.*, *117*, D00V06, doi:10.1029/2011JD016766.

Liang, Q., L. Jaeglé, D. A. Jaffe, P. Weiss-Penzias, A. Heckman, and J. A. Snow (2004), Long-range transport of Asian pollution to the northeast Pacific: Seasonal variations and transport pathways of carbon monoxide, *J. Geophys. Res.*, *109*, D23S07, doi:10.1029/2003JD004402.

Lin, J. J., and H.-S. Tai (2001), Concentrations and distributions of carbonaceous species in ambient particles in Kaohsiung City, Taiwan, *Atmos. Environ.*, *35*(15), 2627–2636, doi:10.1016/S1352-2310(00)00444-1.

Liu, H., D. J. Jacob, I. Bey, R. M. Yantosca, B. N. Duncan, and G. W. Sachse (2003), Transport pathways for Asian pollution outflow over the Pacific: Interannual and seasonal variations, *J. Geophys. Res.*, *108*(D20), 8786, doi:10.1029/2002JD003102.

Lu, R., and R. P. Turco (1994), Air pollutant transport in a coastal environment. Part 1: Two-dimensional simulations of sea-breeze and mountain effects, *J. Atmos. Sci.*, *51*(15), 2285–2308, doi:10.1175/1520-0469(1994)051<2285:APTIAC>2.0.CO;2.

Lu, R., and R. P. Turco (1995), Air pollutant transport in a coastal environment–II. Three-dimensional simulations over Los Angeles Basin, *Atmos. Environ.*, *29*(13), 1499–1518, doi:10.1016/1352-2310(95)00015-Q.

Marr, L. C., and R. A. Harley (2002), Spectral analysis of weekday–weekend differences in ambient ozone, nitrogen oxide, and non-methane hydrocarbon time series in California, *Atmos. Environ.*, *36*(14), 2327–2335, doi:10.1016/S1352-2310(02)00188-7.

McMeeking, G. R., et al. (2010), Black carbon measurements in the boundary layer over western and northern Europe, *Atmos. Chem. Phys.*, *10*, 9393–9414, doi:10.5194/acp-10-9393-2010.

Menon, S., J. Hansen, L. Nazarenko, and Y. Luo (2002), Climate effects of black carbon aerosols in China and India, *Science*, *297*(5590), 2250–2253, doi:10.1126/science.1075159.

Mikhailov, E. F., S. S. Vlasenko, I. A. Podgorny, V. Ramanathan, and C. E. Corrigan (2006), Optical properties of soot–water drop agglomerates: An experimental study, *J. Geophys. Res.*, *111*, D07209, doi:10.1029/2005JD006389.

Modey, W. K., Y. Pang, N. L. Eatough, and D. J. Eatough (2001), Fine particulate ($PM_{2.5}$) composition in Atlanta, USA: Assessment of the particle concentrator-Brigham Young University organic sampling system, PC-BOSS, during the EPA supersite study, *Atmos. Environ.*, *35*(36), 6493–6502, doi:10.1016/S1352-2310(01)00402-2.

Moore, G. E., S. G. Douglas, R. C. Kessler, and J. P. Killus (1991), Identification and tracking of polluted air masses in the South-Central Coast Air Basin, *J. Appl. Meteorol.*, *30*(5), 715–732, doi:10.1175/1520-0450(1991)030<0715:IATOPA>2.0.CO;2.

Moteki, N., and Y. Kondo (2007), Effects of mixing state on black carbon measurements by laser-induced incandescence, *Aerosol Sci. Technol.*, *41*(4), 398–417, doi:10.1080/02786820701199728.

Moteki, N., and Y. Kondo (2010), Dependence of laser-induced incandescence on physical properties of black carbon aerosols: Measurements and theoretical interpretation, *Aerosol Sci. Technol.*, *44*(8), 663–675, doi:10.1080/02786826.2010.484450.

Moteki, N., et al. (2007), Evolution of mixing state of black carbon particles: Aircraft measurements over the western Pacific in March 2004, *Geophys. Res. Lett.*, *34*, L11803, doi:10.1029/2006GL028943.

Murphy, S. M., et al. (2009), Comprehensive simultaneous shipboard and airborne characterization of exhaust from a modern container ship at sea, *Environ. Sci. Technol.*, *43*(13), 4626–4640, doi:10.1021/es802413j.

Nehrkorn, T., J. Eluszkiewicz, S. C. Wofsy, J. C. Lin, C. Gerbig, M. Longo, and S. Freitas (2010), Coupled Weather Research and Forecasting–Stochastic Time-Inverted Lagrangian Transport (WRF-STILT) model, *Meteorol. Atmos. Phys.*, *107*, 51–64, doi:10.1007/s00703-010-0068-x.

Neiburger, M. (1969), The role of meteorology in the study and control of air pollution, *Bull. Am. Meteorol. Soc.*, *50*(12), 957–965.

Offenberg, J., and J. Baker (2000), Aerosol size distributions of elemental and organic carbon in urban and over-water atmospheres, *Atmos. Environ.*, *34*(10), 1509–1517, doi:10.1016/S1352-2310(99)00412-4.

Ohta, S., and T. Okita (1990), A chemical characterization of atmospheric aerosol in Sapporo, *Atmos. Environ., Part A*, *24*(4), 815–822, doi:10.1016/0960-1686(90)90282-R.

Ohta, S., M. Hori, S. Yamagata, and N. Murao (1998), Chemical characterization of atmospheric fine particles in Sapporo with determination of water content, *Atmos. Environ.*, *32*(6), 1021–1025, doi:10.1016/S1352-2310(97)00347-6.

Paatero, P., and U. Tapper (1993), Analysis of different modes of factor analysis as least squares fit problems, *Chemom. Intell. Lab. Syst.*, *18*(2), 183–194, doi:10.1016/0169-7439(93)80055-M.

Palau, J. L., G. Pérez-Landa, J. Meliá, D. Segarra, and M. M. Millán (2006), A study of dispersion in complex terrain under winter conditions using high-resolution mesoscale and Lagrangian particle models, *Atmos. Chem. Phys.*, *6*, 1105–1134, doi:10.5194/acp-6-1105-2006.

Park, K., D. B. Kittelson, and P. H. McMurry (2004), Structural properties of diesel exhaust particles measured by transmission electron microscopy (TEM): Relationships to particle mass and mobility, *Aerosol Sci. Technol.*, *38*(9), 881–889, doi:10.1080/027868290505189.

Park, S. S., Y. J. Kim, and K. Fung (2001), Characteristics of $PM_{2.5}$ carbonaceous aerosol in the Sihwa industrial area, South Korea, *Atmos. Environ.*, *35*, 657–665, doi:10.1016/S1352-2310(00)00357-5.

Paterson, K. G., J. L. Sagady, D. L. Hooper, S. B. Bertman, M. A. Carroll, and P. B. Shepson (1999), Analysis of air quality data using positive matrix factorization, *Environ. Sci. Technol.*, *33*(4), 635–641, doi:10.1021/es980605j.

Pollack, I. B., et al. (2012), Airborne and ground-based observations of a weekend effect in ozone, precursors, and oxidation products in the California South Coast Air Basin, *J. Geophys. Res.*, *117*, D00V05, doi:10.1029/2011JD016772.

Pósfai, M., J. R. Anderson, P. R. Buseck, and H. Sievering (1999), Soot and sulfate aerosol particles in the remote marine troposphere, *J. Geophys. Res.*, *104*(D17), 21,685–21,693, doi:10.1029/1999JD900208.

Pratsinis, S. E., M. D. Zeldin, and E. C. Ellis (1988), Source resolution of the fine carbonaceous aerosol by principal component-stepwise regression analysis, *Environ. Sci. Technol.*, *22*(2), 212–216, doi:10.1021/es00167a013.

Pueschel, R. F., D. F. Blake, K. G. Snetsinger, A. D. A. Hansen, S. Verma, and K. Kato (1992), Black carbon (soot) aerosol in the lower stratosphere and upper troposphere, *Geophys. Res. Lett.*, *19*(16), 1659–1662, doi:10.1029/92GL02478.

Raga, G., T. Castro, and D. Baumgardner (2001), The impact of megacity pollution on local climate and implications for the regional environment: Mexico City, *Atmos. Environ.*, *35*(10), 1805–1811, doi:10.1016/S1352-2310(00)00275-2.

Ramana, M. V., V. Ramanathan, Y. Feng, S.-C. Yoon, S.-W. Kim, G. R. Carmichael, and J. J. Schauer (2010), Warming influenced by the ratio of black carbon to sulphate and the black-carbon source, *Nat. Geosci.*, *3*(8), 542–545, doi:10.1038/ngeo918.

Ramanathan, V., and G. Carmichael (2008), Global and regional climate changes due to black carbon, *Nat. Geosci.*, *1*(4), 221–227, doi:10.1038/ngeo156.

Ramanathan, V., M. V. Ramana, G. Roberts, D. Kim, C. Corrigan, C. Chung, and D. Winker (2007), Warming trends in Asia amplified by brown cloud solar absorption, *Nature*, *448*(7153), 575–578, doi:10.1038/nature06019.

Reche, C., et al. (2011), New considerations for PM, black carbon and particle number concentration for air quality monitoring across different European cities, *Atmos. Chem. Phys.*, *11*, 6207–6227, doi:10.5194/acp-11-6207-2011.

Riemer, N., H. Vogel, and B. Vogel (2004), Soot aging time scales in polluted regions during day and night, *Atmos. Chem. Phys.*, *4*, 1885–1893, doi:10.5194/acp-4-1885-2004.

Robinson, E. (1952), Some air pollution aspects of the Los Angeles temperature inversion, *Bull. Am. Meteorol. Soc.*, *33*(6), 247–250.

Ruellan, S., and H. Cachier (2001), Characterisation of fresh particulate vehicular exhausts near a Paris high flow road, *Atmos. Environ.*, *35*(2), 453–468, doi:10.1016/S1352-2310(00)00110-2.

Schauer, J. J., W. F. Rogge, L. M. Hildemann, M. A. Mazurek, G. R. Cass, and B. R. T. Simoneit (1996), Source apportionment of airborne particulate matter using organic compounds as tracers, *Atmos. Environ.*, *30*(22), 3837–3855, doi:10.1016/1352-2310(96)00085-4.

Schnaiter, M., C. Linke, O. Möhler, K. Naumann, H. Saathoff, R. Wagner, U. Schurath, and B. Wehner (2005), Absorption amplification of black carbon internally mixed with secondary organic aerosol, *J. Geophys. Res.*, *110*, D19204, doi:10.1029/2005JD006046.

Schwarz, J. P., et al. (2006), Single-particle measurements of midlatitude black carbon and light-scattering aerosols from the boundary layer to the lower stratosphere, *J. Geophys. Res.*, *111*, D16207, doi:10.1029/2006JD007076.

Schwarz, J. P., et al. (2008a), Measurement of the mixing state, mass, and optical size of individual black carbon particles in urban and biomass burning emissions, *Geophys. Res. Lett.*, *35*, L13810, doi:10.1029/2008GL033968.

Schwarz, J. P., et al. (2008b), Coatings and their enhancement of black carbon light absorption in the tropical atmosphere, *J. Geophys. Res.*, *113*, D03203, doi:10.1029/2007JD009042.

Schwarz, J. P., et al. (2010), The detection efficiency of the single particle soot photometer, *Aerosol Sci. Technol.*, *44*(8), 612–628, doi:10.1080/02786826.2010.481298.

Seinfeld, J. H., and S. N. Pandis (2006), *Atmospheric Chemistry and Physics: From Air Pollution to Climate Change*, 2nd ed., John Wiley, Hoboken, N. J.

Shiraiwa, M., Y. Kondo, N. Moteki, N. Takegawa, Y. Miyazaki, and D. R. Blake (2007), Evolution of mixing state of black carbon in polluted air from Tokyo, *Geophys. Res. Lett.*, *34*, L16803, doi:10.1029/2007GL029819.

Shiraiwa, M., Y. Kondo, N. Moteki, N. Takegawa, L. K. Sahu, A. Takami, S. Hatakeyama, S. Yonemura, and D. R. Blake (2008), Radiative impact of mixing state of black carbon aerosol in Asian outflow, *J. Geophys. Res.*, *113*, D24210, doi:10.1029/2008JD010546.

Slowik, J. G., et al. (2007), An inter-comparison of instruments measuring black carbon content of soot particles, *Aerosol Sci. Technol.*, *41*(3), 295–314, doi:10.1080/02786820701197078.

Stelson, A. W. (1990), Urban aerosol refractive index prediction by partial molar refraction approach, *Environ. Sci. Technol.*, *24*(11), 1676–1679, doi:10.1021/es00081a008.

Stephens, M., N. Turner, and J. Sandberg (2003), Particle identification by laser-induced incandescence in a solid-state laser cavity, *Appl. Opt.*, *42*(19), 3726–3736, doi:10.1364/AO.42.003726.

Stier, P., J. H. Seinfeld, S. Kinne, and O. Boucher (2007), Aerosol absorption and radiative forcing, *Atmos. Chem. Phys.*, *7*, 5237–5261, doi:10.5194/acp-7-5237-2007.

Stohl, A., C. Forster, A. Frank, P. Seibert, and G. Wotawa (2005), Technical note: The Lagrangian particle dispersion model FLEXPART version 6.2, *Atmos. Chem. Phys.*, *5*, 2461–2474, doi:10.5194/acp-5-2461-2005.

Stolzenburg, M., N. Kreisberg, and S. Hering (1998), Atmospheric size distributions measured by differential mobility optical particle size spectrometry, *Aerosol Sci. Technol.*, *29*(5), 402–418, doi:10.1080/02786829808965579.

Subramanian, R., et al. (2010), Black carbon over Mexico: The effect of atmospheric transport on mixing state, mass absorption cross-section, and BC/CO ratios, *Atmos. Chem. Phys.*, *10*, 219–237, doi:10.5194/acp-10-219-2010.

Sullivan, A. P., R. E. Peltier, C. A. Brock, J. A. de Gouw, J. S. Holloway, C. Warneke, A. G. Wollny, and R. J. Weber (2006), Airborne measurements of carbonaceous aerosol soluble in water over northeastern United States: Method development and an investigation into water-soluble organic carbon sources, *J. Geophys. Res.*, *111*, D23S46, doi:10.1029/2006JD007072.

Toon, O. B., and T. P. Ackerman (1981), Algorithms for the calculation of scattering by stratified spheres, *Appl. Opt.*, *20*(20), 3657–3660, doi:10.1364/AO.20.003657.

Tripathi, S. N., S. Dey, V. Tare, and S. K. Satheesh (2005), Aerosol black carbon radiative forcing at an industrial city in northern India, *Geophys. Res. Lett.*, *32*, L08802, doi:10.1029/2005GL022515.

Turpin, B. J., and J. J. Huntzicker (1991), Secondary formation of organic aerosol in the Los Angeles basin: A descriptive analysis of organic and elemental carbon concentrations, *Atmos. Environ., Part A*, *25*(2), 207–215, doi:10.1016/0960-1686(91)90291-E.

Turpin, B. J., and J. J. Huntzicker (1995), Identification of secondary organic aerosol episodes and quantitation of primary and secondary organic aerosol concentrations during SCAQS, *Atmos. Environ.*, *29*(23), 3527–3544, doi:10.1016/1352-2310(94)00276-Q.

Turpin, B. J., and H.-J. Lim (2001), Species contributions to PM2.5 mass concentrations: Revisiting common assumptions for estimating organic mass, *Aerosol Sci. Technol.*, *35*(1), 602–610, doi:10.1080/02786820119445.

Turpin, B. J., J. J. Huntzicker, S. M. Larson, and G. R. Cass (1991), Los Angeles summer midday particulate carbon: Primary and secondary aerosol, *Environ. Sci. Technol.*, *25*(10), 1788–1793, doi:10.1021/es00022a017.

Ulbrich, I. M., M. R. Canagaratna, Q. Zhang, D. R. Worsnop, and J. L. Jimenez (2009), Interpretation of organic components from positive matrix factorization of aerosol mass spectrometric data, *Atmos. Chem. Phys.*, *9*, 2891–2918, doi:10.5194/acp-9-2891-2009.

Venkataraman, C., C. K. Reddy, S. Josson, and M. S. Reddy (2002), Aerosol size and chemical characteristics at Mumbai, India, during the INDOEX-IFP (1999), *Atmos. Environ.*, *36*(12), 1979–1991, doi:10.1016/S1352-2310(02)00167-X.

Wakimoto, R. M., and J. L. McElroy (1986), Lidar observation of elevated pollution layers over Los Angeles, *J. Clim. Appl. Meteorol.*, *25*(11), 1583–1599, doi:10.1175/1520-0450(1986)025<1583:LOOEPL>2.0.CO;2.

Weingartner, E., H. Burtscher, and U. Baltensperger (1997), Hygroscopic properties of carbon and diesel soot particles, *Atmos. Environ.*, *31*(15), 2311–2327, doi:10.1016/S1352-2310(97)00023-X.

Wonaschütz, A., S. P. Hersey, A. Sorooshian, J. S. Craven, A. R. Metcalf, R. C. Flagan, and J. H. Seinfeld (2011), Impact of a large wildfire on water-soluble organic aerosol in a major urban area: The 2009 Station Fire in Los Angeles County, *Atmos. Chem. Phys.*, *11*, 8257–8270, doi:10.5194/acp-11-8257-2011.

Zappoli, S., et al. (1999), Inorganic, organic and macromolecular components of fine aerosol in different areas of Europe in relation to their water solubility, *Atmos. Environ.*, *33*(17), 2733–2743, doi:10.1016/S1352-2310(98)00362-8.

Zarzycki, C. M., and T. C. Bond (2010), How much can the vertical distribution of black carbon affect its global direct radiative forcing?, *Geophys. Res. Lett.*, *37*, L20807, doi:10.1029/2010GL044555.

Zhang, Q., et al. (2007), Ubiquity and dominance of oxygenated species in organic aerosols in anthropogenically-influenced Northern Hemisphere midlatitudes, *Geophys. Res. Lett.*, *34*, L13801, doi:10.1029/2007GL029979.

Zier, M. (1991), Mass concentrations of total dust and soot in the near surface air in East Germany, *J. Aerosol Sci.*, *22*(S1), S597–S600, doi:10.1016/S0021-8502(05)80172-7.

W. Angevine and J. Brioude, Chemical Sciences Division, NOAA Earth System Research Laboratory, 325 Broadway, Mail Stop R/CSD4, Boulder, CO 80305, USA.

J. S. Craven, J. J. Ensberg, R. C. Flagan, A. R. Metcalf, and J. H. Seinfeld, Division of Chemistry and Chemical Engineering, California Institute of Technology, 1200 E. California Blvd., Mail Code 210-41, Pasadena, CA 91125, USA. (metcalf@caltech.edu; seinfeld@caltech.edu)

H. T. Duong and A. Sorooshian, Department of Chemical and Environmental Engineering, University of Arizona, PO Box 210011, Tucson, AZ 85721, USA.

H. H. Jonsson, Center for Interdisciplinary Remotely-Piloted Aircraft Studies, Naval Postgraduate School, Monterey, CA 93943, USA.